On a fully three-dimensional bending analysis of very thick smart composite cube-like bulk structures

Mohammad Malikan [a,b], Shahriar Dastjerdi [c], Victor A. Eremeyev [a,d,*], Mehran Kadkhodayan [c]

[a] Department of Mechanics of Materials and Structures, Faculty of Civil and Environmental Engineering, Gdańsk University of Technology, ul. Gabriela Narutowicza 11/12, Gdańsk 80-233, Poland
[b] Department of Plastics Engineering, University of Massachusetts Lowell, 1 University Ave, Lowell, Massachusetts 01854, USA
[c] Department of Mechanical Engineering, Ferdowsi University of Mashhad, Mashhad 91775-1111, Iran
[d] Department of Civil and Environmental Engineering and Architecture(DICAAR), University of Cagliari, via Marengo, 2, Cagliari 09123, Italy

ARTICLE INFO

ABSTRACT

Here we discuss the behaviour of very thick composite plates considering electro-magneto-elastic coupling of various types using fully three-dimensional (3D) kinematics. Published research highlights a lack of studies on the 3D mechanics of smart composite plates that integrate both higher-order (flexoelectric/flexomagnetic) and lower-order (piezoelectric/piezomagnetic) multiple physical fields (electro-magneto-elastic). The common approach to achieving the targeted and desired mechanical behavior within such composites could involve using structural elements. This gap can potentially be addressed by amalgamating the term $\partial/\partial z$ with the 2D governing equations of plates. This expression indicates alterations in thickness, in which z is the coordinate dedicated to the thickness. The governing equations can be created by operating on the variational method which enables us to establish and settle the 3D bending equations of the bulk structure. The pointed-out equations have been influenced by the implementation of additional hypotheses, such as von Kármán's strain and complicated 3D tensor relations. Inserting the term $\partial/\partial z$ into the mathematical model renders that the analytical solution techniques are unable to assist us in obtaining numerical results. Consequently, a semi-analytical solving method grounded on the polynomial phrases facilitates the acquisition of the required solution. This fully 3D bending study of very thick piezocomposite cube-like bulk structures (CBS) can be an original reference in the field of mechanics of intelligent plate-like structures.

1. Introduction

Among the capabilities of smart materials, one can mention their ability to maintain their original configuration. However, such a property is under certain conditions due to special stimuli. This outstanding feature shows the upper hand for smart composite materials in contrast to other composite structures [1–3]. The intelligent materials are able to sense different environmental circumstances and respond to these situations due to their atomic and perovskite crystalline structure. Among the conditions, one can refer to humidity, magnetic, and electric fields, and also thermal environment [4].

From a commercial point of view, intelligent composite structures are famous for electromagnetic materials, which among the cases of their role in sensitive engineering industries can be expressed as tools that are used as actuators and sensors. Designing and producing non-

biological systems inspired by biological systems is one of the purposes used for this type of material. In fact, mathematical and computational modeling, analysis, and simulation of processes in complex biological mechanisms are made possible by these intelligent structures. Smart composite plates are among the commonly operated elements in electromagnetic industries. The outstanding advantages of these engineering pieces bring a wide range of applications. These composites provide the beneficial mechanical properties of classic composites obtained from the combination of several natural substances, together with the smart features all at once. Several basic engineering materials are involved in the formation of these composites, including microstructure materials or even smaller ones, i.e. nanostructures. The combination of primary materials such as cobalt, iron oxide, lead, etc., can result in smart ceramics that provide significant sensing capability. In the initial process of ceramic production, after crystallization at a temperature higher than Curie, the perovskite crystal structure is formed. This

* Corresponding author.
E-mail address: eremeyev.victor@gmail.com (V.A. Eremeyev).

Nomenclature

$\aleph$	Displacement vectors
$u_i (i = 1, 2, 3)$	Displacements in the x-, y-, and z- directions of the domain
V	Domain's volume
N^0_{xx} and N^0_{yy}	Effect of magnetic field in line with the x- and y-axis
ε_{ij}	Elastic strains
σ_{ij}	Elastic stresses
ψ	External magnetic potential
F	External mass loads
h_{ijkl}	4th-order converse flexomagnetic tensor
f_{ijkl}	4th-order direct flexomagnetic tensor
C_{ijkl}	4th-order elasticity tensor
$\Re$	Free energy density
η_{ijk}	Gradient of the elastic strains
ξ_{ijk}	Higher-order stress tensor
T_{ij}	Hyper stress resultant
δ_{ij}	Kronecker's delta
q	Lateral static load
x	Length coordinate
L_x	Length of the CBS
H_i	Magnetic field
B_i	Magnetic flux
l	Material's length scale parameter
Ψ	Magnetic potential function
ν	Poisson's ratio
α	Position vector
G	Shear modulus
U	Strain energy
t	Surface traction
a_{ij}	2nd-order magnetic permeability tensor
g_{ijklmn}	6th-order strain gradient tensor
g_i	Strain gradient coefficients
q_{ijk}	3rd-order piezomagnetic tensor
z	Thickness coordinate
h	Thickness of the CBS
u, v, and w	3D displacements for x-, y-, and z-axis
∇	3D nabla operator
R	Unknown variables for displacements
N_{xx}	Work done by a magnetic field
W	Work performed by external forces
L_y	Width of the CBS
E	Young's modulus

combination of materials magically gives the ability to be intelligent and enables engineers to use these ceramics in control systems, actuators, and sensors on any scale [5–9]. The utilization of the substances is evident across diverse applications, aiming to manage structural shape, mitigate noise, and eradicate vibrations in various items such as aerospace engineering, marine industries, and mechanical fields. Further, assort of functions can be witnessed in other domains, ranging from automotive and civil platforms, specifically in green energy sectors [10–14].

The Smartness aspect can be acquired through the medium of various effects such as piezomagneticity, piezoelectricity, and higher order ones like flexoelectricity and flexomagneticity among which the last item is a cutting-edge and fresh research territory. Flexomagnetic effect (FM) encompasses an essential characteristic through which a substance demonstrates a reactive magnetic behavior, either as a reverse response due to interaction between elastic strains and magnetic field gradients, or through the interrelation of elastic strain gradients and magnetic fields which results in the emergence of the direct effect. The phenomenon of FM is contingent upon size, showcasing its significance primarily at reduced scales, particularly within the realms of micro and nano dimensions. Consequently, ceramics crafted at these diminutive scales prominently manifest the effect associated with FM. This property harbors the capability to significantly transform various domains including but not limited to spintronics, magnetoelasticity, etc., potentially revolutionizing their methodologies and applications. Continued exploration within this research area holds the promise of innovating novel material features with heightened magnetic characteristics which allow us to precisely control and manipulate via elastic displacements [15–24].

While the FM influence comprehension remains nascent in theory, a significant portion of research involves computational models. Nevertheless, empirical investigations have yielded compelling evidence affirming the effect's existence [15–24]. Ongoing advancements for this category are poised to usher in a wave of innovative materials and devices harnessing the FM effect which opens pathways to novel technological avenues and promising fresh prospects for the development of cutting-edge technologies. The research emphasis has been on flexomagnetic properties across diverse material conditions while delving into the underlying circumstances that dictate their mechanical response within one- (1D) and two-dimensional (2D) investigations [25–34]. The presented references offer an excellent foundation for acquainting oneself with the FM, serving as valuable resources to comprehend the current status and ongoing research in this field. All the above-mentioned research backgrounds are the sight of 2D mechanical studies approving further research which is necessary for the FM effect to thoroughly understand the capacity of structures consisting of flexomagnetic influence. However, in the immediate past, [35] kept forward the FM studies by modeling the smart composite beams in a 3D medium. They realized that a 3D computational model could provide more meaningfulness for strain gradients, magnetic fields, etc. Although this work developed the research on FM, it relates to the beam structures. The present study grants another computational model to present full deformations in three axes for a 3D intelligent CBS entailing FM.

This article comprehensively delves into the fully three-dimensional elasticity analysis of FM smart CBS, integrating the authors' novel derivation of the modified energy density for piezomagnetic-flexomagnetic (PFM) structures. The subsequent section systematically unfolds the constitutive equations while consolidating 3D tensors sourced from reputable literature. As the formulation addresses variable thickness CBS, derivation of internal moments and forces remains unattainable; however, direct acquisition of principal equations via stress components is proposed. Assumedly, a uniformly distributed transverse static load is applied, prompting the exploration of potential solutions to the 3D constitutive relations by means of polynomial terms utilizing a semi-analytical approach.

To lay out this article, it has been arranged in the following sequence: The initial section, Section 1, aims to provide an introductory overview of the subject matter along with a concise review of pertinent literature. Section 2 is dedicated to elucidating the mathematical model governing the primary focus of this study as outlined in the title. Within Section 3, an in-depth exploration of semi-analytical solution methodology is represented which provides insight into the technique employed for resolving the problem. Section 4 meticulously examines the obtained numerical results by validating them with established references. Section 5 precisely explores the acquired findings by offering an elaborate analysis and comprehensive interpretation of the results. Finally, a conclusion section that summarily shortens the carried-out study is assigned to this paper by Section 6.
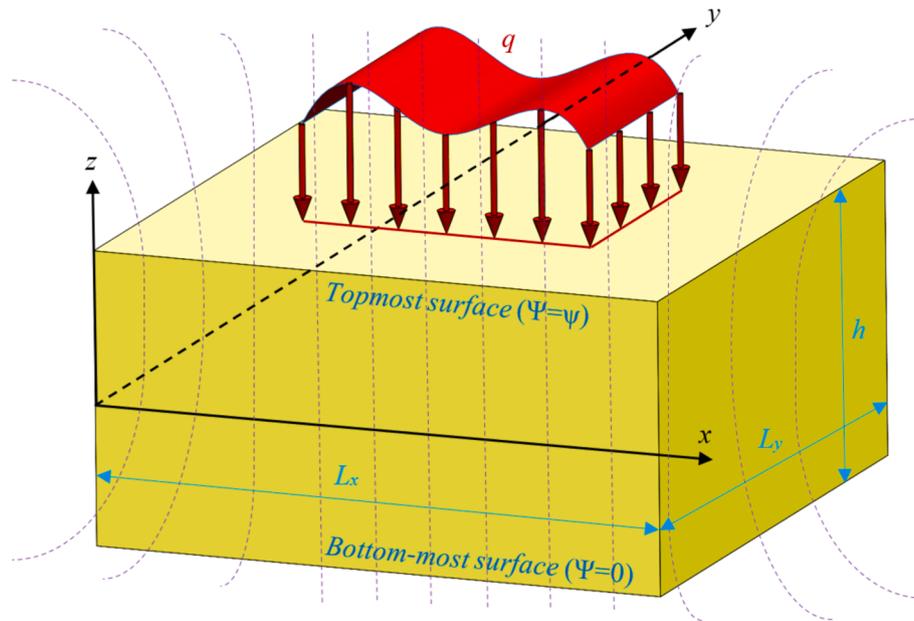
Fig. 1. A 3D multi-physic composite CBS under an uniform lateral static load surrounded by a vertical magnetic field.

2. Mathematical modeling

Upon the groundwork of the rectangular coordinate system, Fig. 1 vividly illustrates a smart cube-like bulk structure (CBS) encompassing a pre-volume with dimensions of $[0, L_x] \times [0, L_y] \times [-0.5 h, 0.5 h]$, confronted with a linear magnetic field and a transverse static load. It is emphasized that the variables "L_x" and "L_y" represent the effective length and width of the CBS in all relations. And "h" denotes the initial thickness of the undeformed CBS.

2.1. The PFM model

It is conceivable to succinctly explore the mathematical model pertaining to PFM structures as documented by Malikan and Eremeyev [28]. The fundamental equations integrating piezomagnetic and FM effects can be found in detail in the corresponding reference. The problem can be linked to the characteristic equations of static bending utilizing the variational principle [36–39].

In the subsequent phase of the mathematical modeling, all relationships are going to be derived to suit a thick CBS with a fully 3D structure. The vectors of displacements possess the following configuration [40–42]

$$\begin{bmatrix} u_1(x,y,z) \\ u_2(x,y,z) \\ u_3(x,y,z) \end{bmatrix} = \begin{bmatrix} u(x,y,z) \\ v(x,y,z) \\ w(x,y,z) \end{bmatrix} \tag{1}$$

As seen above, no assumption has been made for kinematic displacements and this is a merit of 3D elasticity. With the help of the Lagrange strain formula, one can derive the elastic strains, and subsequently computing the strain gradients is a straightforward process [43–45]

$$\varepsilon_{ij} = \frac{1}{2}\left(\frac{\partial u_i}{\partial x_j} + \frac{\partial u_j}{\partial x_i}\right); \ i,j,k = 1,2,3 \tag{2a}$$

$$\eta_{ijk} = \frac{\partial}{\partial x_k}[\varepsilon_{ij}]; \ i,j,k = 1,2,3 \tag{2b}$$

Following that, matrices representing the strain gradient and strains themselves can be generated as

$$[\varepsilon] = \begin{bmatrix} \varepsilon_{xx} & \varepsilon_{xy} & \varepsilon_{xz} \\ \varepsilon_{yx} & \varepsilon_{yy} & \varepsilon_{yz} \\ \varepsilon_{zx} & \varepsilon_{zy} & \varepsilon_{zz} \end{bmatrix} \tag{3a}$$

$$[\eta] = \begin{bmatrix} (\eta_{xxx} \ \eta_{xxy} \ \eta_{xxz}) & (\eta_{xyx} \ \eta_{xyy} \ \eta_{xyz}) & (\eta_{xzx} \ \eta_{xzy} \ \eta_{xzz}) \\ (\eta_{yxx} \ \eta_{yxy} \ \eta_{yxz}) & (\eta_{yyy} \ \eta_{yyx} \ \eta_{yyz}) & (\eta_{yzx} \ \eta_{yzy} \ \eta_{yzz}) \\ (\eta_{zxx} \ \eta_{zxy} \ \eta_{zxz}) & (\eta_{zyx} \ \eta_{zyy} \ \eta_{zyz}) & (\eta_{zzx} \ \eta_{zzy} \ \eta_{zzz}) \end{bmatrix} \tag{3b}$$

In this particular case, the tensor of strains and their gradients exhibit symmetry indicated as $\varepsilon_{ij} = \varepsilon_{ji}$ and $\eta_{ijk} = \eta_{jik}$. Hence, one obtains

$$\begin{Bmatrix} \varepsilon_{xx} \\ \varepsilon_{yy} \\ \varepsilon_{zz} \end{Bmatrix} = \begin{Bmatrix} \frac{\partial u}{\partial x} \\ \frac{\partial v}{\partial y} \\ \frac{\partial w}{\partial z} \end{Bmatrix} \begin{Bmatrix} \varepsilon_{yz} \\ \varepsilon_{xz} \\ \varepsilon_{xy} \end{Bmatrix} = \begin{Bmatrix} \varepsilon_{zy} \\ \varepsilon_{zx} \\ \varepsilon_{yx} \end{Bmatrix} = \begin{Bmatrix} \frac{1}{2}\left(\frac{\partial v}{\partial z} + \frac{\partial w}{\partial y}\right) \\ \frac{1}{2}\left(\frac{\partial u}{\partial z} + \frac{\partial w}{\partial x}\right) \\ \frac{1}{2}\left(\frac{\partial u}{\partial y} + \frac{\partial v}{\partial x}\right) \end{Bmatrix} \tag{4}$$

In sequence, we arrived at the formulas

$$\begin{Bmatrix} \eta_{xxx} \\ \eta_{xxy} \\ \eta_{xxz} \end{Bmatrix} = \begin{Bmatrix} \frac{\partial \varepsilon_{xx}}{\partial x} \\ \frac{\partial \varepsilon_{xx}}{\partial y} \\ \frac{\partial \varepsilon_{xx}}{\partial z} \end{Bmatrix} = \begin{Bmatrix} \frac{\partial^2 u}{\partial x^2} \\ \frac{\partial^2 u}{\partial x \partial y} \\ \frac{\partial^2 u}{\partial x \partial z} \end{Bmatrix} \begin{Bmatrix} \eta_{yyx} \\ \eta_{yyy} \\ \eta_{yyz} \end{Bmatrix} = \begin{Bmatrix} \frac{\partial \varepsilon_{yy}}{\partial x} \\ \frac{\partial \varepsilon_{yy}}{\partial y} \\ \frac{\partial \varepsilon_{yy}}{\partial z} \end{Bmatrix}$$

$$= \begin{Bmatrix} \frac{\partial^2 v}{\partial x \partial y} \\ \frac{\partial^2 v}{\partial y^2} \\ \frac{\partial^2 v}{\partial y \partial z} \end{Bmatrix} \begin{Bmatrix} \eta_{zzx} \\ \eta_{zzy} \\ \eta_{zzz} \end{Bmatrix} = \begin{Bmatrix} \frac{\partial \varepsilon_{zz}}{\partial x} \\ \frac{\partial \varepsilon_{zz}}{\partial y} \\ \frac{\partial \varepsilon_{zz}}{\partial z} \end{Bmatrix} = \begin{Bmatrix} \frac{\partial^2 w}{\partial x \partial z} \\ \frac{\partial^2 w}{\partial y \partial z} \\ \frac{\partial^2 w}{\partial z^2} \end{Bmatrix}$$
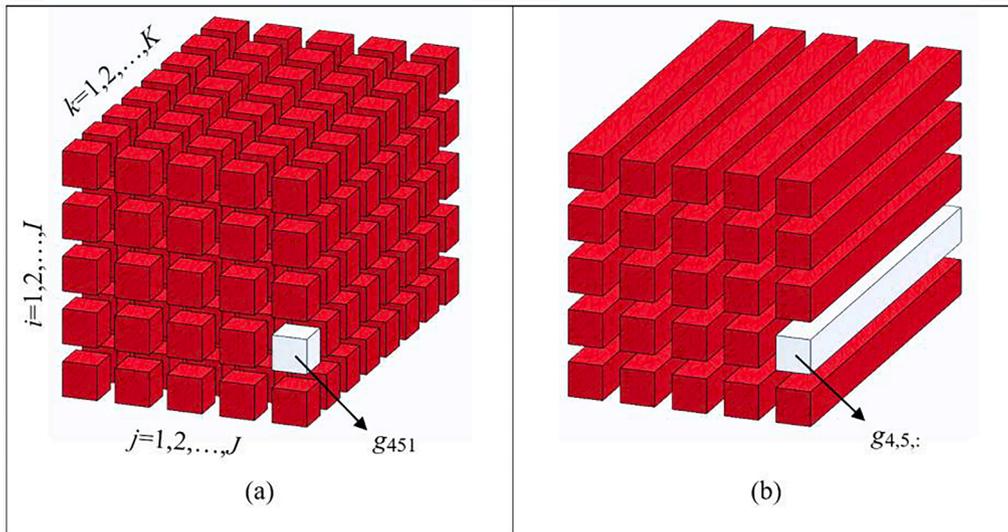
Fig. 2. A 3D presentation of the strain gradient tensor (a); and the tube-mode mixture (b).

$$\left\{ \begin{array}{c} \eta_{xzx} \\ \eta_{xzy} \\ \eta_{xzz} \end{array} \right\} = \left\{ \begin{array}{c} \dfrac{\partial \varepsilon_{xz}}{\partial x} \\[6pt] \dfrac{\partial \varepsilon_{xz}}{\partial y} \\[6pt] \dfrac{\partial \varepsilon_{xz}}{\partial z} \end{array} \right\} = \dfrac{1}{2} \left\{ \begin{array}{c} \dfrac{\partial^2 u}{\partial x \partial z} + \dfrac{\partial^2 w}{\partial x^2} \\[6pt] \dfrac{\partial^2 u}{\partial y \partial z} + \dfrac{\partial^2 w}{\partial x \partial y} \\[6pt] \dfrac{\partial^2 u}{\partial z^2} + \dfrac{\partial^2 w}{\partial x \partial z} \end{array} \right\} \left\{ \begin{array}{c} \eta_{yzx} \\ \eta_{yzy} \\ \eta_{yzz} \end{array} \right\} = \left\{ \begin{array}{c} \dfrac{\partial \varepsilon_{yz}}{\partial x} \\[6pt] \dfrac{\partial \varepsilon_{yz}}{\partial y} \\[6pt] \dfrac{\partial \varepsilon_{yz}}{\partial z} \end{array} \right\}$$

$$= \dfrac{1}{2} \left\{ \begin{array}{c} \dfrac{\partial^2 v}{\partial x \partial z} + \dfrac{\partial^2 w}{\partial x \partial y} \\[6pt] \dfrac{\partial^2 v}{\partial y \partial z} + \dfrac{\partial^2 w}{\partial y^2} \\[6pt] \dfrac{\partial^2 v}{\partial z^2} + \dfrac{\partial^2 w}{\partial y \partial z} \end{array} \right\}$$

It is seriously a challenge to encounter a 3D tensor and convert it to a 2D writable one. Not to mention that we here developed the 3D strain gradient tensor (η_{ijk}) ($g \in \mathbb{R}^{I \times J \times K}$) visualized similarly to Rubik's cube and based on the tube-mode composition method (Fig. 2) [46]. Necessarily, applying symmetry rules finalizes the tensor.

It is currently anticipated to produce constitutive equations utilizing the formula provided in [28].

$$\delta U + \delta W = 0 \tag{6}$$

For the current intentions, the changes in strain energy are written as

$$\delta U^{All} = \delta U^{Mech} + \delta U^{Mag} \tag{7}$$

in which the acronyms "Mag" and "Mech" respectively represent the magnetic and mechanical components within the energy context.

Expressing the alteration of the mechanical segment involves gathering the non-zero tensors, which can be formulated as

$$\delta U^{Mech} = \int_V \left[\begin{array}{c} \sigma_{xx}\delta\varepsilon_{xx} + \sigma_{yy}\delta\varepsilon_{yy} + \sigma_{zz}\delta\varepsilon_{zz} + \tau_{yz}\delta\gamma_{yz} + \tau_{xz}\delta\gamma_{xz} + \tau_{xy}\delta\gamma_{xy} \\ +\xi_{xxx}\delta\eta_{xxx} + \xi_{xxy}\delta\eta_{xxy} + \xi_{xxz}\delta\eta_{xxz} + \xi_{yyx}\delta\eta_{yyx} + \xi_{yyy}\delta\eta_{yyy} + \xi_{yyz}\delta\eta_{yyz} \\ +\xi_{zzx}\delta\eta_{zzx} + \xi_{zzy}\delta\eta_{zzy} + \xi_{zzz}\delta\eta_{zzz} + \xi_{yzx}\delta\eta_{yzx} + \xi_{yzy}\delta\eta_{yzy} + \xi_{yzz}\delta\eta_{yzz} \\ +\xi_{xzx}\delta\eta_{xzx} + \xi_{xzy}\delta\eta_{xzy} + \xi_{xzz}\delta\eta_{xzz} + \xi_{xyx}\delta\eta_{xyx} + \xi_{xyy}\delta\eta_{xyy} + \xi_{xyz}\delta\eta_{xyz} \end{array} \right] dV \tag{8a}$$

$$\left\{ \begin{array}{c} \eta_{xyx} \\ \eta_{xyy} \\ \eta_{xyz} \end{array} \right\} = \left\{ \begin{array}{c} \dfrac{\partial \varepsilon_{xy}}{\partial x} \\[6pt] \dfrac{\partial \varepsilon_{xy}}{\partial y} \\[6pt] \dfrac{\partial \varepsilon_{xy}}{\partial z} \end{array} \right\} = \dfrac{1}{2} \left\{ \begin{array}{c} \dfrac{\partial^2 u}{\partial x \partial y} + \dfrac{\partial^2 v}{\partial x^2} \\[6pt] \dfrac{\partial^2 u}{\partial y^2} + \dfrac{\partial^2 v}{\partial x \partial y} \\[6pt] \dfrac{\partial^2 u}{\partial y \partial z} + \dfrac{\partial^2 v}{\partial x \partial z} \end{array} \right\} \left\{ \begin{array}{c} \eta_{zyx} \\ \eta_{zyy} \\ \eta_{zyz} \end{array} \right\} = \left\{ \begin{array}{c} \dfrac{\partial \varepsilon_{zy}}{\partial x} \\[6pt] \dfrac{\partial \varepsilon_{zy}}{\partial y} \\[6pt] \dfrac{\partial \varepsilon_{zy}}{\partial z} \end{array} \right\} = \left\{ \begin{array}{c} \eta_{yzx} \\ \eta_{yzy} \\ \eta_{yzz} \end{array} \right\}$$

$$\left\{ \begin{array}{c} \eta_{zxx} \\ \eta_{zxy} \\ \eta_{zxz} \end{array} \right\} = \left\{ \begin{array}{c} \dfrac{\partial \varepsilon_{zx}}{\partial x} \\[6pt] \dfrac{\partial \varepsilon_{zx}}{\partial y} \\[6pt] \dfrac{\partial \varepsilon_{zx}}{\partial z} \end{array} \right\} = \left\{ \begin{array}{c} \eta_{xzx} \\ \eta_{xzy} \\ \eta_{xzz} \end{array} \right\} \left\{ \begin{array}{c} \eta_{yxx} \\ \eta_{yxy} \\ \eta_{yxz} \end{array} \right\} = \left\{ \begin{array}{c} \dfrac{\partial \varepsilon_{yx}}{\partial x} \\[6pt] \dfrac{\partial \varepsilon_{yx}}{\partial y} \\[6pt] \dfrac{\partial \varepsilon_{yx}}{\partial z} \end{array} \right\} = \left\{ \begin{array}{c} \eta_{xyx} \\ \eta_{xyy} \\ \eta_{xyz} \end{array} \right\} \tag{5}$$

$$\delta U^{Mag} = \int_V \left[\begin{array}{c} -T_{xx}\delta\partial H_x/\partial x - T_{yy}\delta\partial H_y/\partial y - T_{zz}\delta\partial H_z/\partial z \\ -B_x\delta H_x - B_y\delta H_y - B_z\delta H_z \end{array} \right] dV \tag{8b}$$

where

$$H_k = \{ H_x \quad H_y \quad H_z \} = -\left\{ \dfrac{\partial \Psi}{\partial x} \quad \dfrac{\partial \Psi}{\partial y} \quad \dfrac{\partial \Psi}{\partial z} \right\} \tag{9}$$

It should be borne in mind that Eq. (9) can also be presented as a diagonal matrix [35].

The energy variation for elastic and magnetic parts can be

$$\delta U^{Mech} = \int_0^{L_x} \int_0^{L_y} \int_{-h/2}^{h/2} \begin{bmatrix} \sigma_{xx}\left(\dfrac{\partial \delta u}{\partial x}\right) + \sigma_{yy}\left(\dfrac{\partial \delta v}{\partial y}\right) + \sigma_{zz}\left(\dfrac{\partial \delta u}{\partial z}\right) + \tau_{yz}\left(\dfrac{\partial \delta v}{\partial z} + \dfrac{\partial \delta w}{\partial y}\right) + \tau_{xz}\left(\dfrac{\partial \delta u}{\partial z} + \dfrac{\partial \delta w}{\partial x}\right) \\ +\tau_{xy}\left(\dfrac{\partial \delta u}{\partial y} + \dfrac{\partial \delta v}{\partial x}\right) + \xi_{xxx}\left(\dfrac{\partial^2 \delta u}{\partial x^2}\right) + \xi_{xxy}\left(\dfrac{\partial^2 \delta u}{\partial x \partial y}\right) + \xi_{xxz}\left(\dfrac{\partial^2 \delta u}{\partial x \partial z}\right) + \xi_{yyx}\left(\dfrac{\partial^2 \delta v}{\partial x \partial y}\right) \\ +\xi_{yyy}\left(\dfrac{\partial^2 \delta v}{\partial y^2}\right) + \xi_{yyz}\left(\dfrac{\partial^2 \delta v}{\partial y \partial z}\right) + \xi_{zzx}\left(\dfrac{\partial^2 \delta w}{\partial x \partial z}\right) + \xi_{zzy}\left(\dfrac{\partial^2 \delta w}{\partial y \partial z}\right) + \xi_{zzz}\left(\dfrac{\partial^2 \delta w}{\partial z^2}\right) \\ +\xi_{yzx}\left(\dfrac{\partial^2 \delta v}{\partial x \partial z} + \dfrac{\partial^2 \delta w}{\partial x \partial y}\right) + \xi_{yzy}\left(\dfrac{\partial^2 \delta v}{\partial y \partial z} + \dfrac{\partial^2 \delta w}{\partial y^2}\right) + \xi_{yzz}\left(\dfrac{\partial^2 \delta v}{\partial z^2} + \dfrac{\partial^2 \delta w}{\partial y \partial z}\right) \\ +\xi_{xzx}\left(\dfrac{\partial^2 \delta u}{\partial x \partial z} + \dfrac{\partial^2 \delta w}{\partial x^2}\right) + \xi_{xzy}\left(\dfrac{\partial^2 \delta u}{\partial y \partial z} + \dfrac{\partial^2 \delta w}{\partial x \partial y}\right) + \xi_{xzz}\left(\dfrac{\partial^2 \delta u}{\partial z^2} + \dfrac{\partial^2 \delta w}{\partial x \partial z}\right) \\ +\xi_{xyx}\left(\dfrac{\partial^2 \delta u}{\partial x \partial y} + \dfrac{\partial^2 \delta v}{\partial x^2}\right) + \xi_{xyy}\left(\dfrac{\partial^2 \delta u}{\partial y^2} + \dfrac{\partial^2 \delta v}{\partial x \partial y}\right) + \xi_{xyz}\left(\dfrac{\partial^2 \delta u}{\partial y \partial z} + \dfrac{\partial^2 \delta v}{\partial x \partial z}\right) \end{bmatrix} dz\,dy\,dx \tag{10}$$

$$\delta U^{Mag} = -\int_0^{L_x} \int_0^{L_y} \int_{-h/2}^{h/2} \left(\frac{\partial B_x}{\partial x} + \frac{\partial B_y}{\partial y} + \frac{\partial B_z}{\partial z} + \frac{\partial^2 T_{xx}}{\partial x^2} + \frac{\partial^2 T_{yy}}{\partial y^2} + \frac{\partial^2 T_{zz}}{\partial z^2}\right) \delta\Psi\,dz\,dy\,dx$$
$$+\int_0^{L_y} \int_{-h/2}^{h/2} \left[B_x + \frac{\partial T_{xx}}{\partial x}\right]_0^{L_x} \delta\Psi\,dz\,dy + \int_0^{L_x} \int_{-h/2}^{h/2} \left[B_y + \frac{\partial T_{yy}}{\partial y}\right]_0^{L_y} \delta\Psi\,dz\,dx$$
$$+\int_0^{L_x} \int_0^{L_y} \left[B_z + \frac{\partial T_{zz}}{\partial z}\right]_{-h/2}^{h/2} \delta\Psi\,dy\,dx \tag{11}$$

The work which is performed by the magnetic field is

$$\delta W = \int_0^{L_x} \int_0^{L_y} \left[N_{xx}^0\left(\frac{\partial \delta w}{\partial x}\frac{\partial w}{\partial x}\right) + N_{yy}^0\left(\frac{\partial \delta w}{\partial y}\frac{\partial w}{\partial y}\right)\right] dy\,dx \tag{12}$$

It is necessary to note that the shear effect of the external in-plane force is not taken into the model.

Using the fundamental lemma of the calculus of variations one can collect terms in Eq. (10), leading to establishing linear 3D bending equations as

$$\delta u : 0 \rightarrow \frac{\partial \sigma_{xx}}{\partial x} + \frac{\partial \tau_{xy}}{\partial y} + \frac{\partial \tau_{xz}}{\partial z} + \frac{\partial^2 \xi_{xxx}}{\partial x^2} + \frac{\partial^2 \xi_{xxy}}{\partial x \partial y} + \frac{\partial^2 \xi_{xxz}}{\partial x \partial z} + \frac{\partial^2 \xi_{xzx}}{\partial x \partial z} + \frac{\partial^2 \xi_{xzy}}{\partial y \partial z} + \frac{\partial^2 \xi_{xzz}}{\partial z^2}$$
$$+ \frac{\partial^2 \xi_{xyx}}{\partial x \partial y} + \frac{\partial^2 \xi_{xyy}}{\partial y^2} + \frac{\partial^2 \xi_{xyz}}{\partial y \partial z} = 0 \tag{13a}$$

$$\delta v : 0 \rightarrow \frac{\partial \sigma_{yy}}{\partial y} + \frac{\partial \tau_{xy}}{\partial x} + \frac{\partial \tau_{yz}}{\partial z} + \frac{\partial^2 \xi_{yyy}}{\partial y^2} + \frac{\partial^2 \xi_{yyx}}{\partial x \partial y} + \frac{\partial^2 \xi_{yyz}}{\partial y \partial z} + \frac{\partial^2 \xi_{yzx}}{\partial x \partial z} + \frac{\partial^2 \xi_{yzy}}{\partial y \partial z} + \frac{\partial^2 \xi_{yzz}}{\partial z^2}$$
$$+ \frac{\partial^2 \xi_{xyy}}{\partial x \partial y} + \frac{\partial^2 \xi_{yyx}}{\partial x^2} + \frac{\partial^2 \xi_{xyz}}{\partial x \partial z} = 0 \tag{13b}$$

$$\delta w : 0 \rightarrow \frac{\partial \sigma_{xx}}{\partial x}\frac{\partial w}{\partial x} + \frac{\partial \sigma_{zz}}{\partial z} + \sigma_{xx}\frac{\partial^2 w}{\partial x^2} + \sigma_{yy}\frac{\partial^2 w}{\partial y^2} + \sigma_{zz}\frac{\partial^2 w}{\partial z^2} + \frac{\partial \tau_{xz}}{\partial x} + \frac{\partial \tau_{yz}}{\partial y}$$
$$+2\tau_{xy}\frac{\partial^2 w}{\partial x \partial y} + 2\tau_{xz}\frac{\partial^2 w}{\partial x \partial z} + 2\tau_{yz}\frac{\partial^2 w}{\partial y \partial z} + 2\xi_{xxx}\frac{\partial^3 w}{\partial x^3} + \frac{\partial^2 \xi_{xxx}}{\partial x^2} + \frac{\partial^2 \xi_{zzz}}{\partial z^2} + \frac{\partial^2 \xi_{zzx}}{\partial x \partial z}$$
$$+\frac{\partial^2 \xi_{xzz}}{\partial x \partial z} + \frac{\partial^2 \xi_{zzy}}{\partial y \partial z} + \frac{\partial^2 \xi_{xzy}}{\partial x \partial y} + \frac{\partial^2 \xi_{yzx}}{\partial x \partial y} + \frac{\partial^2 \xi_{yzy}}{\partial y^2} + \frac{\partial^2 \xi_{yzz}}{\partial y \partial z} + N_{xx}^0\frac{\partial^2 w}{\partial x^2} + N_{yy}^0\frac{\partial^2 w}{\partial y^2} = 0 \tag{13c}$$

The tensor reduction is contingent upon the structure which maintains a linear-elastic behavior and exhibits a plane of elastic symmetry, enabling the further reduction of independent elastic constants from C_{ijkl} to C_{ij} ($i,j \in \{1, 2, \ldots, 6\}$) [47–52] as

$$[C_{ijkl}] = \begin{bmatrix} C_{1111} & C_{1122} & C_{1133} & 0 & 0 & 0 \\ C_{1122} & C_{2222} & C_{2233} & 0 & 0 & 0 \\ C_{1133} & C_{2233} & C_{3333} & 0 & 0 & 0 \\ 0 & 0 & 0 & C_{2323} & 0 & 0 \\ 0 & 0 & 0 & 0 & C_{1313} & 0 \\ 0 & 0 & 0 & 0 & 0 & C_{1212} \end{bmatrix} \tag{14}$$

The six-order strain gradient tensor can be decreased into

$$[g_{ijklmn}] = \begin{bmatrix} g_{1111} & g_{1122} & g_{1133} & g_{1123} & g_{1113} & g_{1112} \\ g_{2211} & g_{2222} & g_{2233} & g_{2223} & g_{2213} & g_{2212} \\ g_{3311} & g_{3322} & g_{3333} & g_{3323} & g_{3313} & g_{3312} \\ g_{2311} & g_{2322} & g_{2333} & g_{2323} & g_{2313} & g_{2312} \\ g_{1311} & g_{1322} & g_{1333} & g_{1323} & g_{1313} & g_{1312} \\ g_{1211} & g_{1222} & g_{1233} & g_{1223} & g_{1213} & g_{1212} \end{bmatrix} \tag{15}$$

The tensor of piezomagnetic properties can be condensed or simplified into a more compact form if the piezomagnetic material possesses a hexagonal crystal [42,50]

$$[q_{ijk}] = \begin{bmatrix} q_{11} & q_{12} & q_{13} & q_{14} & q_{15} & q_{16} \\ q_{21} & q_{22} & q_{23} & q_{24} & q_{25} & q_{26} \\ q_{31} & q_{32} & q_{33} & q_{34} & q_{35} & q_{36} \end{bmatrix} \tag{16}$$

wherein the piezomagnetic constants underwent a transformation, shifting from the initial q_{ijk} notation into $q_{i\alpha}$ ($\alpha \in \{1, 2, \ldots, 6\}$) and considering $q_{24} = q_{15}$ [35].

Likewise, the symmetry variations of the reverse and the direct impacts of the FM can be streamlined into distinct components f_{11}, f_{111}, and f_{14} particularly tailored for a crystal structure with a cubic shape [49,51,52]

$$[f_{ij}] = \begin{bmatrix} 0 & 0 & 0 & 0 & f_{111} & 0 \\ 0 & 0 & 0 & f_{111} & 0 & 0 \\ f_{14} & f_{14} & f_{11} & 0 & 0 & 0 \end{bmatrix} \tag{17}$$

Subsequently, due to limited available literature on the material, assuming an equivalence between the converse FM tensor and the direct one, it is hypothesized that the former can be simplified accordingly, particularly considering the diagnosed cubic crystal nature of the piezomagnetic material.
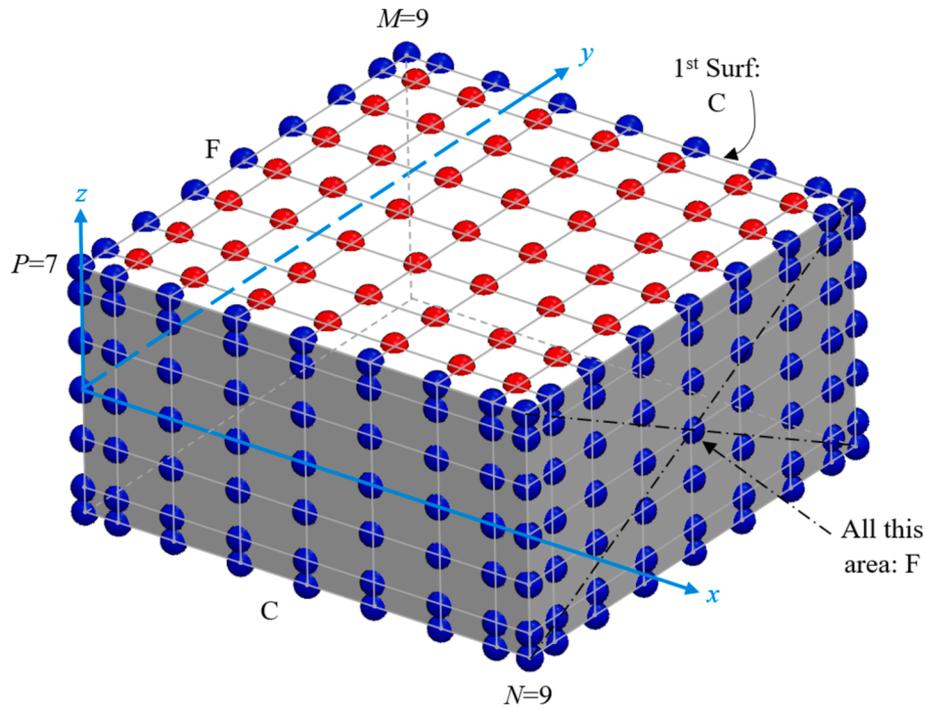
Fig. 3. CGL grid points for a CBS (N = 9, M = 9, P = 7) with an example for boundary conditions CFCF.

$$[h_{ij}] = \begin{bmatrix} 0 & 0 & 0 & 0 & h_{46} & 0 \\ 0 & 0 & 0 & h_{46} & 0 & 0 \\ h_{15} & h_{15} & h_{11} & 0 & 0 & 0 \end{bmatrix} \tag{18}$$

The intricate challenge of size dependence inherent in smart devices has been meticulously addressed by leveraging various micro-mathematical models, as outlined in the works by [53–55]. The current research focuses on the first-strain gradient theory to deploy scale impact under the context of the generalized model. Notably, a comprehensive formulation has been precisely derived for linear elastic and isotropic materials and the tensor of rank six of strain gradient (g_{ijklmn}), drawing insights from the research contributions of [34,56–60]

$$\begin{aligned} g_{ijklmn} = &g_1 \left[\left(\delta_{ij}\delta_{kl} + \delta_{ik}\delta_{jl} \right)\delta_{mn} + \left(\delta_{im}\delta_{ln} + \delta_{in}\delta_{lm} \right)\delta_{jk} \right] \\ &+ g_2 \left[\delta_{ij} \left(\delta_{km}\delta_{ln} + \delta_{kn}\delta_{lm} \right) + \delta_{ik} \left(\delta_{jn}\delta_{lm} + \delta_{jm}\delta_{ln} \right) \right] + g_3\delta_{il}\delta_{jk}\delta_{mn} \\ &+ g_4\delta_{il} \left(\delta_{jm}\delta_{kn} + \delta_{jn}\delta_{km} \right) + g_5 \left[\delta_{im} \left(\delta_{jl}\delta_{kn} + \delta_{jn}\delta_{kl} \right) + \delta_{in} \left(\delta_{jl}\delta_{km} + \delta_{jm}\delta_{kl} \right) \right] \end{aligned} \tag{19}$$

A higher-order elastic moduli, denoted by the symbol g_i is introduced inside Eq. (19). It is crucial to note that the material under scrutiny is a non-centrosymmetric PM substance. Nevertheless, a simplification is here made by means of a centrosymmetric tensor for strain gradient. This choice has been merely an assumption stemming from the lack of adequate literature in this field, compelling its implementation. The constituents of the strain gradient tensor (g) are obtained from gradient elasticity with isotropy, employing the order-of-differentiation conditions as

$$\delta_{ij} = \begin{cases} 1, if \ \text{i} \ = \ \text{j}, \\ 0, if \ \text{i} \neq \text{j}. \end{cases} \tag{20}$$

Therefore, as an illustration, the first member of the strain gradient tensor can be articulated utilizing the principles of the Voigt notation in a subsequent manner

$$g_{11} = 4(g_1 + g_2 + g_5) + g_3 + 2g_4 \tag{21}$$

where the g_i displayed earlier is detailed below [34,57,59]

$$g_1 = -\frac{2}{3}(g_2 + g_5) \quad g_2 = \frac{\mu}{30}\left(27l_0^2 - 4l_1^2 - 15l_2^2\right)$$

$$g_3 = \frac{1}{3}(8g_2 + 2g_5) \quad g_4 = \frac{\mu}{3}\left(l_1^2 + 6l_2^2\right) \quad g_5 = \frac{\mu}{3}\left(l_1^2 - 3l_2^2\right)$$

where some additional variables can be seen as l_0, l_1, and l_2, which are here called length scale parameters. It is worth noting that in order to simplify matters, we presume that $l_0 = l_1 = l_2 = l$.

Furthermore, a precise amount for shear modulus (μ) of strain gradient remains undetermined. Consequently, let us assume an equivalent scalar of μ to elastic shear modulus (G) for our current analysis.

We proceed with the development of the formulation. The relationships between stress and strain, accounting for both lower and higher-order effects, can be articulated as follows [28]

$$\begin{Bmatrix} \sigma_{xx} \\ \sigma_{yy} \\ \sigma_{zz} \\ \tau_{yz} \\ \tau_{xz} \\ \tau_{xy} \end{Bmatrix} = \left[C_{ij}\right]_{6\times6} \times \begin{Bmatrix} \varepsilon_{xx} \\ \varepsilon_{yy} \\ \varepsilon_{zz} \\ \gamma_{yz} \\ \gamma_{xz} \\ \gamma_{xy} \end{Bmatrix} - \left[q_{ij}\right]_{6\times3} \times \begin{Bmatrix} H_x \\ H_y \\ H_z \end{Bmatrix} - \left[h_{ij}\right]_{6\times3} \times \begin{Bmatrix} \dfrac{\partial H_x}{\partial x} \\ \dfrac{\partial H_y}{\partial y} \\ \dfrac{\partial H_z}{\partial z} \end{Bmatrix} \tag{22}$$
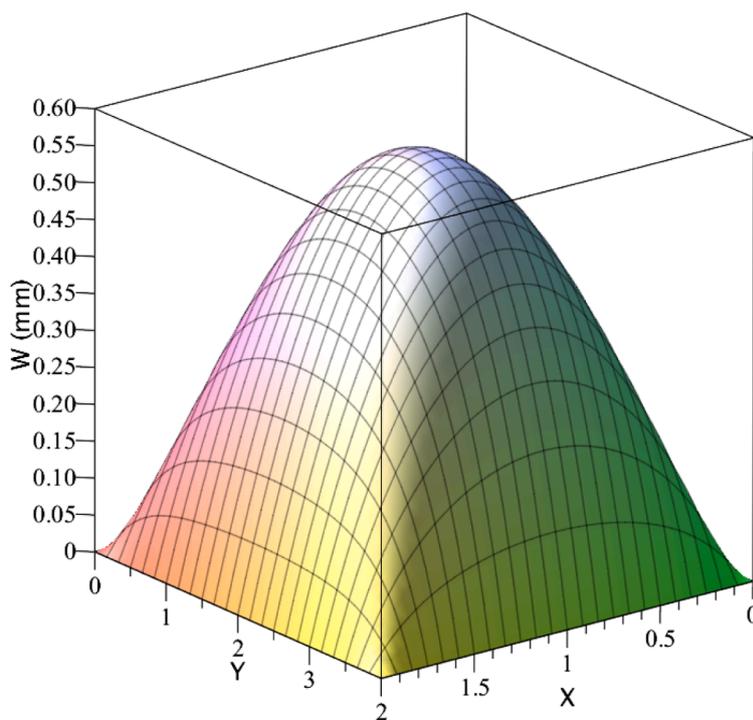
(a)

(b) 5.679e-1mm
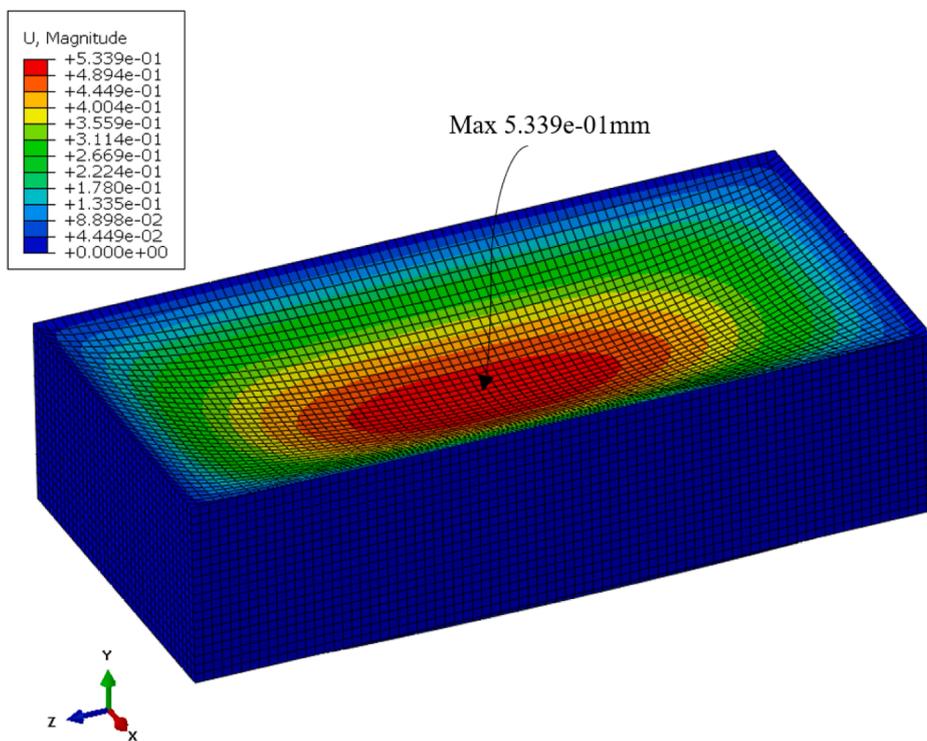
Fig. 4. Validation for the deflection in the top surface of the thick CBS with CCCC (q = 1GPa); (a) Abaqus (b) Present 3D model.

$$\begin{bmatrix} \xi_{xxx} & \xi_{xxy} & \xi_{xxz} \\ \xi_{xyx} & \xi_{xyy} & \xi_{xyz} \\ \xi_{xzx} & \xi_{xzy} & \xi_{xzz} \\ \xi_{yyx} & \xi_{yyy} & \xi_{yyz} \\ \xi_{yzx} & \xi_{yzy} & \xi_{yzz} \\ \xi_{zzx} & \xi_{zzy} & \xi_{zzz} \end{bmatrix} = \left[g_{ij}\right]_{6\times6} \times \begin{bmatrix} \eta_{xxx} & \eta_{xxy} & \eta_{xxz} \\ \eta_{xyx} & \eta_{xyy} & \eta_{xyz} \\ \eta_{xzx} & \eta_{xzy} & \eta_{xzz} \\ \eta_{yyx} & \eta_{yyy} & \eta_{yyz} \\ \eta_{yzx} & \eta_{yzy} & \eta_{yzz} \\ \eta_{zzx} & \eta_{zzy} & \eta_{zzz} \end{bmatrix} - \left[f_{ij}\right]_{6\times3} \times \left\{ \begin{matrix} H_x \\ H_y \\ H_z \end{matrix} \right\}$$

(23)

$$\left\{ \begin{matrix} T_{xx} \\ T_{yy} \\ T_{zz} \end{matrix} \right\} = -\left[h_{ij}\right]_{3\times6} \times \left\{ \begin{matrix} \varepsilon_{xx} \\ \varepsilon_{yy} \\ \varepsilon_{zz} \\ \gamma_{yz} \\ \gamma_{xz} \\ \gamma_{xy} \end{matrix} \right\}$$

(24)

$$\left\{ \begin{matrix} B_x \\ B_y \\ B_z \end{matrix} \right\} = \left[a_{ij}\right]_{3\times3} \times \left\{ \begin{matrix} H_x \\ H_y \\ H_z \end{matrix} \right\} + \left[q_{ij}\right]_{3\times6} \times \left\{ \begin{matrix} \varepsilon_{xx} \\ \varepsilon_{yy} \\ \varepsilon_{zz} \\ \gamma_{yz} \\ \gamma_{xz} \\ \gamma_{xy} \end{matrix} \right\} + \left[f_{ij}\right]_{3\times6}$$

$$\times \begin{bmatrix} \eta_{xxx} & \eta_{xxy} & \eta_{xxz} \\ \eta_{xyx} & \eta_{xyy} & \eta_{xyz} \\ \eta_{xzx} & \eta_{xzy} & \eta_{xzz} \\ \eta_{yyx} & \eta_{yyy} & \eta_{yyz} \\ \eta_{yzx} & \eta_{yzy} & \eta_{yzz} \\ \eta_{zzx} & \eta_{zzy} & \eta_{zzz} \end{bmatrix}$$

(25)

The extended stiffness matrix of three-dimensional elasticity pertaining to an isotropic material with homogeneity is represented [61–65]

$$\left[C_{ijkl}\right] = \begin{bmatrix} \dfrac{E(1-\nu)}{K} & \dfrac{E\nu}{K} & \dfrac{E\nu}{K} & 0 & 0 & 0 \\[2mm] \dfrac{E\nu}{K} & \dfrac{E(1-\nu)}{K} & \dfrac{E\nu}{K} & 0 & 0 & 0 \\[2mm] \dfrac{E\nu}{K} & \dfrac{E\nu}{K} & \dfrac{E(1-\nu)}{K} & 0 & 0 & 0 \\[2mm] 0 & 0 & 0 & \dfrac{E}{2(1+\nu)} & 0 & 0 \\[2mm] 0 & 0 & 0 & 0 & \dfrac{E}{2(1+\nu)} & 0 \\[2mm] 0 & 0 & 0 & 0 & 0 & \dfrac{E}{2(1+\nu)} \end{bmatrix}$$

(26)

in which $K = (1 + \nu)(1 - 2\nu)$.

The work done due to external forces encompasses an impact of the transverse magnetic field, acting as a longitudinal load, thereby influencing the overall mechanical response.
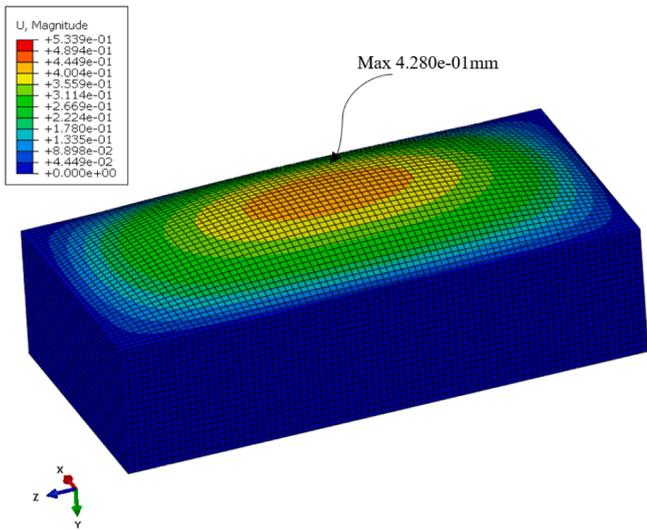
$$\begin{cases} N_{xx}^0 = \dfrac{\psi}{h}q_{31} \\[2mm] N_{yy}^0 = N_{xx}^0 \end{cases}$$

(27)

Establishing the magnetic potential amounts significantly guides our discourse. We will proceed by defining a magnetic potential along the top and bottom thickness surfaces of the CBS [28]
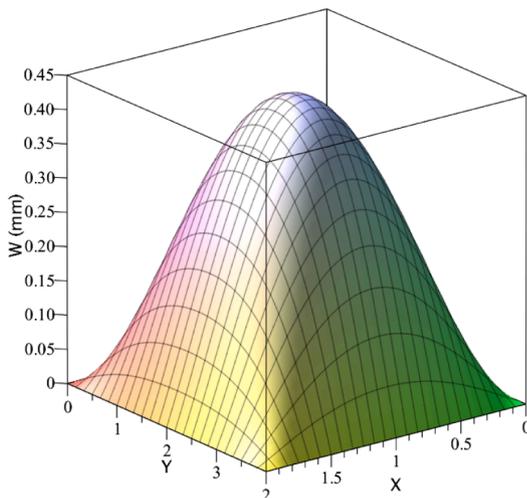
$$\left\{ \begin{matrix} \Psi\left(+\dfrac{h}{2}\right) \\[2mm] \Psi\left(-\dfrac{h}{2}\right) \end{matrix} \right\} = \left\{ \begin{matrix} \psi \\ 0 \end{matrix} \right\}$$

(28)

For the subsequent relations, we will disregard the direct PFM parameter as our focus centers solely on evaluating the converse PFM effect. An exact mathematical correlation between Eq. (9), Eq. (11), Eq. (25), and Eq. (28) yields

$$\Psi = \left(\frac{z^2}{2} - \frac{h^2}{8}\right)\left[\frac{q_{31}}{a_{33}}\left(\frac{\partial^2 u}{\partial x \partial z}\right) + \frac{q_{32}}{a_{33}}\left(\frac{\partial^2 v}{\partial y \partial z}\right) + \frac{q_{33}}{a_{33}}\left(\frac{\partial^2 w}{\partial z^2}\right)\right] + \psi\left(\frac{z}{h} + \frac{1}{2}\right)$$

$$+\left(\frac{z^2}{2} - \frac{h^2}{8}\right)\left\{\frac{h_{46}}{a_{33}}\left(\frac{\partial^3 u}{\partial x^2 \partial z} + \frac{\partial^3 w}{\partial x^3}\right) + \frac{h_{46}}{a_{33}}\left(\frac{\partial^3 v}{\partial y^2 \partial z} + \frac{\partial^3 w}{\partial y^3}\right) + \frac{h_{15}}{a_{33}}\left(\frac{\partial^3 u}{\partial x \partial z^2}\right)\right.$$

$$\left. + \frac{h_{15}}{a_{33}}\left(\frac{\partial^3 v}{\partial y \partial z^2}\right) + \frac{h_{11}}{a_{33}}\left(\frac{\partial^3 w}{\partial z^3}\right)\right\}$$
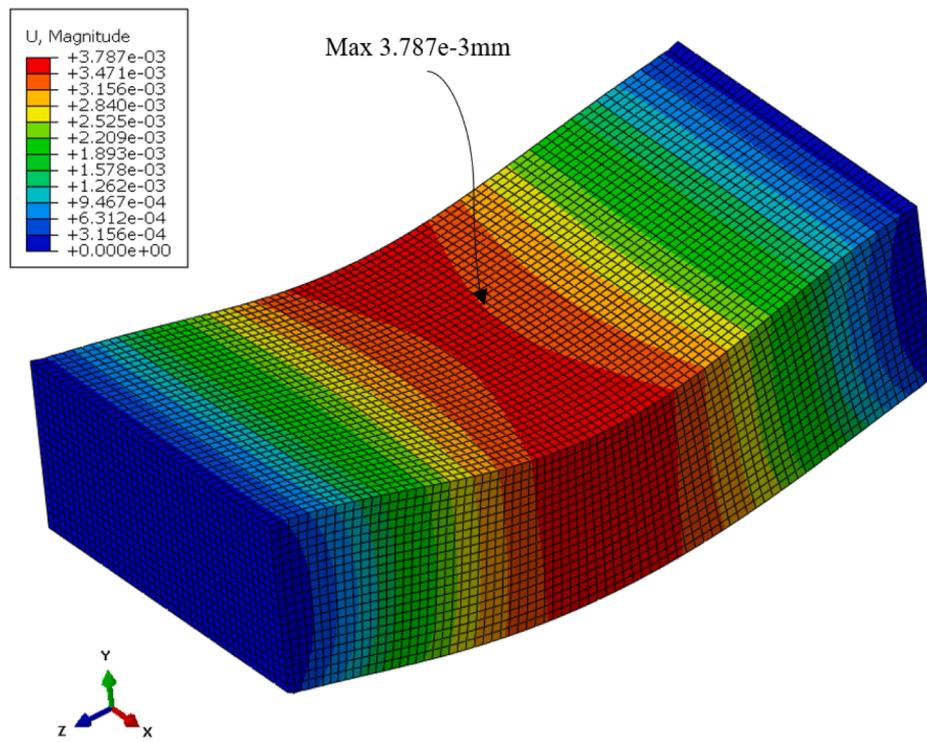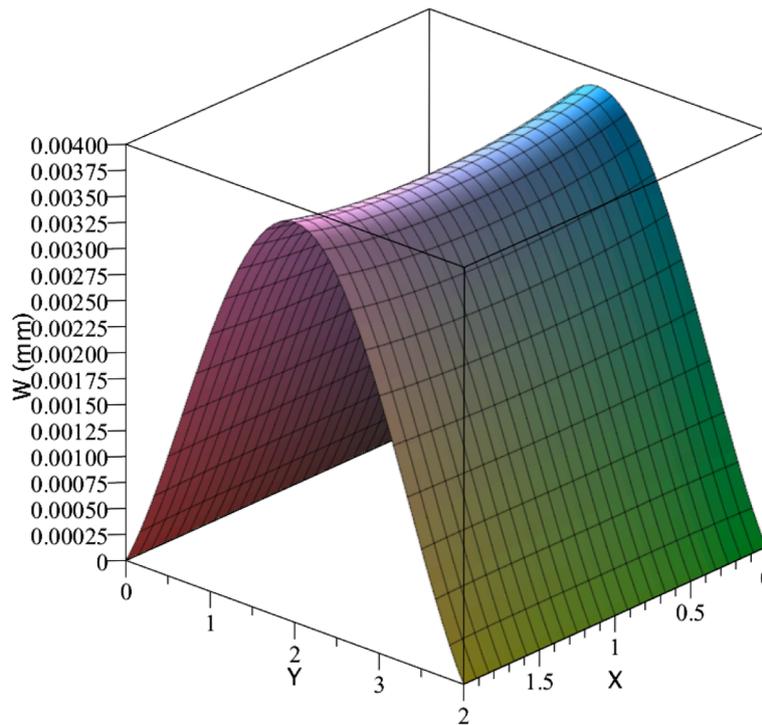
(29)

(a)

(b) 4.421e-1mm

Fig. 5. Validation for the deflection in the bottom surface of the thick CBS with CCCC (q = 1GPa); (a) Abaqus (b) Present 3D model.
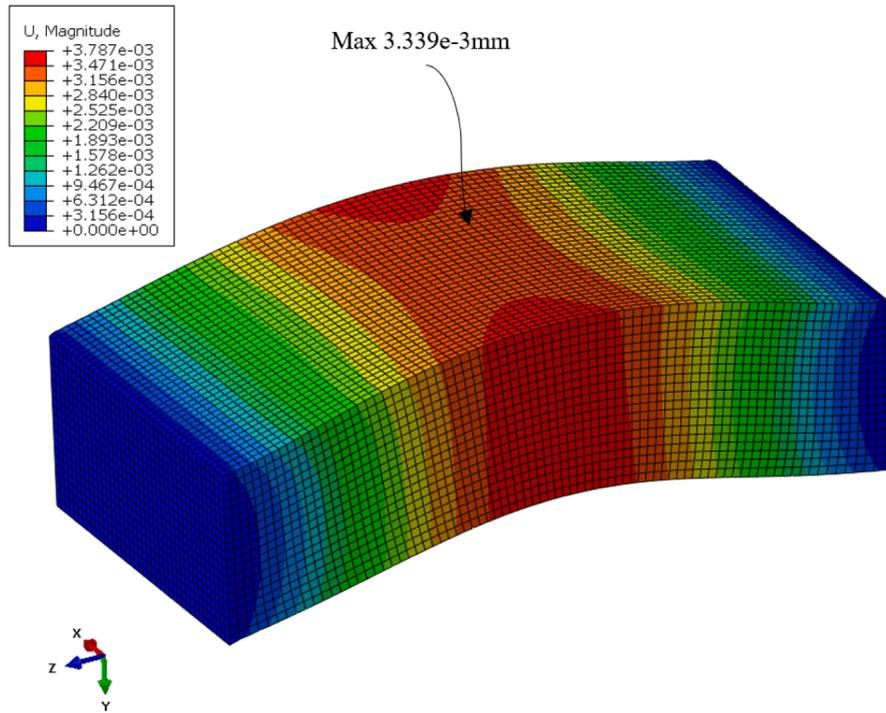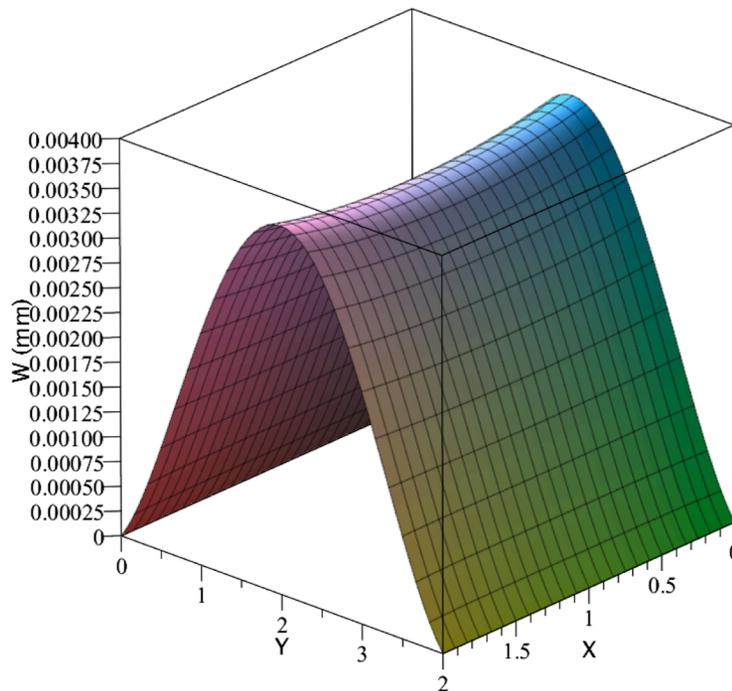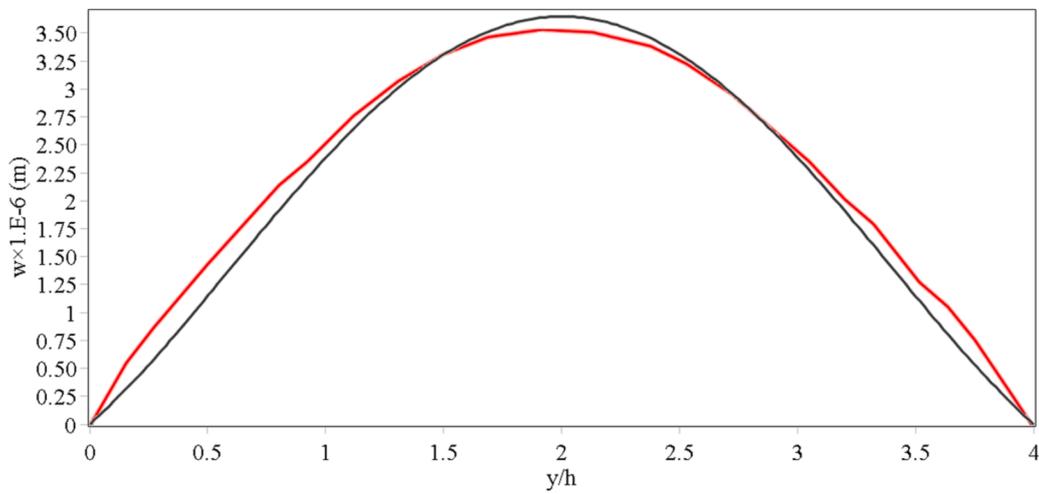
(a)

(b) 3.711e-3mm

Fig. 6. Validation for the deflection in the top surface of the thick CBS with CFCF (q = 1 MPa); (a) Abaqus (b) Present 3D model.

(a)

(b) 3.578e-3mm

Fig. 7. Validation for the deflection in the bottom surface of the thick CBS with CFCF (q = 1 MPa); (a) Abaqus (b) Present 3D model.

Observing the above relation, Eq. (28) truly fulfills the magnetic requisites specified in Eq. (29). Later, by exclusively considering the transverse magnetic field component, we attain the magnetic field. Following extensive mathematical analysis, the governing bending equations can be expanded.

3. Solution technique

A diverse range of techniques have been employed to tackle mathematical and physical issues explicitly by offering practicable solutions. On such methods, semi-analytical solutions like the Semi-Analytical Polynomial Method (SAPM) as detailed by [43,44,63,66–70], facilitate

Fig. 8. Validation for the deflection through the bottom y-axis in the top surface of the thick CBS with CFCF (q = 1 MPa); Abaqus (Red) Present 3D model (black).
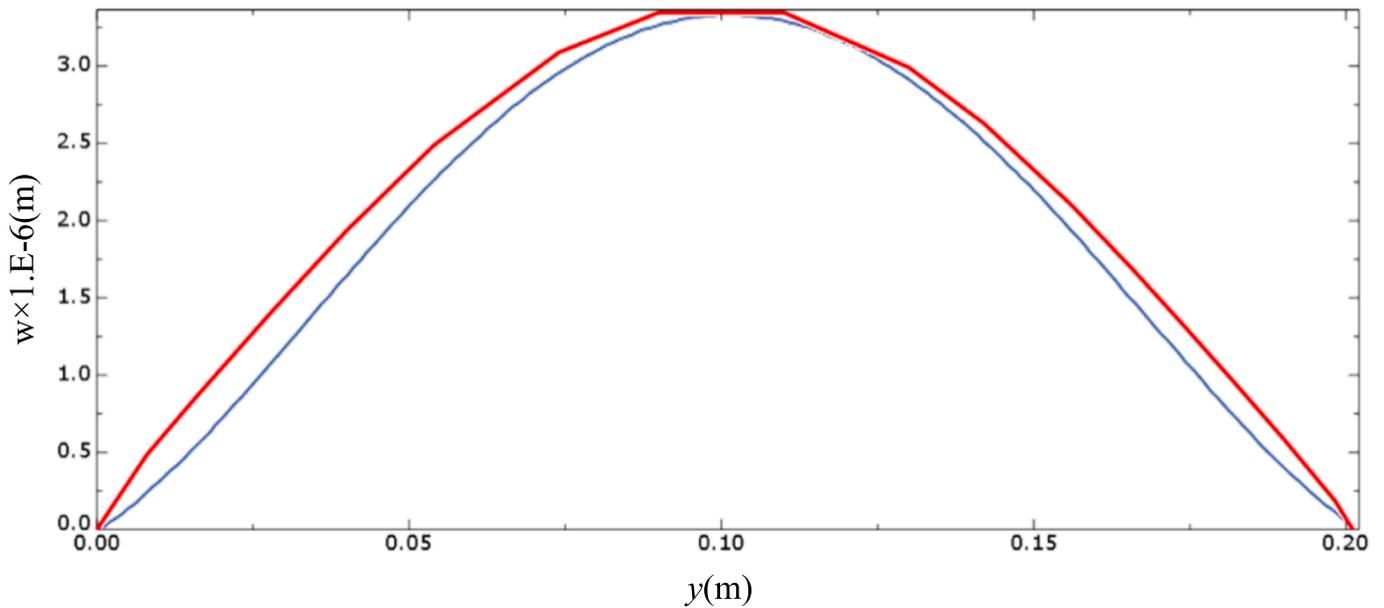
Fig. 9. Validation for the deflection through the y-axis in the bottom surface of the thick CBS with CFCF (q = 1 MPa); Abaqus (Red) Present 3D model (Blue).

swifter and more accessible problem-solving by utilizing functions decomposition into more straightforward forms of polynomial terms. Renowned for its great accuracy, the SAPM technique has gained prominence in addressing various physical challenges by prompting the forthcoming utilization of its 3D adaptation for problem-solving. For further elucidation on the SAPM technique, detailed insights have been available from earlier research [43,44,63,66–70].

First, the governing equations can be checked to ensure their precision and workability. Addedly, as the analysis is a full 3D and a benchmark one, we should guarantee the certainty of the boundary conditions and then provide the goal results. To effectively solve the governing differential equations, one should adhere to the following natural and essential boundary conditions imposed across the CBS borders together with the top and bottom surfaces. The "surf" here means the surface around the CBS and "surf 1" is shown in Fig. 3. Surf 4 is in front of Surf 1, and Surf 2 is on the $x = 0$ in a counterclockwise rotation. Due to the fully 3D model, the edge/boundary area is not a line (2D plate) and we are faced with four surfaces around the CBS, leading to very complicated imposing of the boundary conditions.

• **Clamped (C):**

$$u\big|_{\text{Surf 1 - 4}} = v\big|_{\text{Surf 1 - 4}} = w\big|_{\text{Surf 1 - 4}} = 0$$

• **Free (F):**

$$\sigma_{xx}\big|_{\text{Surf 2,4}} = N_{xx}^0, \sigma_{yy}\big|_{\text{Surf 1,3}} = N_{yy}^0,$$

$$\tau_{xz}\bigg|_{\text{Surf 2,4};z=-\frac{h}{2},+\frac{h}{2}} = \tau_{yz}\bigg|_{\text{Surf 1,3};z=-\frac{h}{2},+\frac{h}{2}} = 0$$

The specified conditions yielding the lower and upper surfaces of the CBS are defined as

Top surface: $\sigma_{zz}\bigg|_{z=+\frac{h}{2}} = Q, \tau_{xz}\bigg|_{z=+\frac{h}{2}} = \tau_{yz}\bigg|_{z=+\frac{h}{2}} = 0$, where $Q = q/b$.

Bottom surface: $\sigma_{zz}\bigg|_{z=-\frac{h}{2}} = \tau_{xz}\bigg|_{z=-\frac{h}{2}} = \tau_{yz}\bigg|_{z=-\frac{h}{2}} = 0$
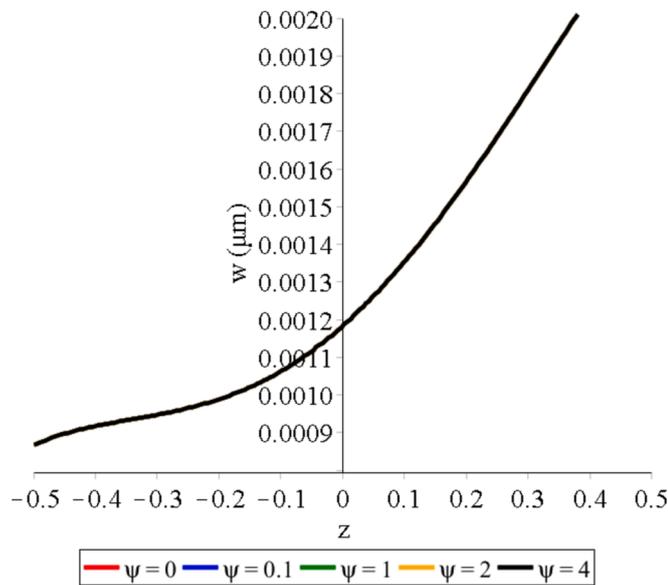
Fig. 10a. Thickness deformations vs. the different magnetic potential for CCCC.
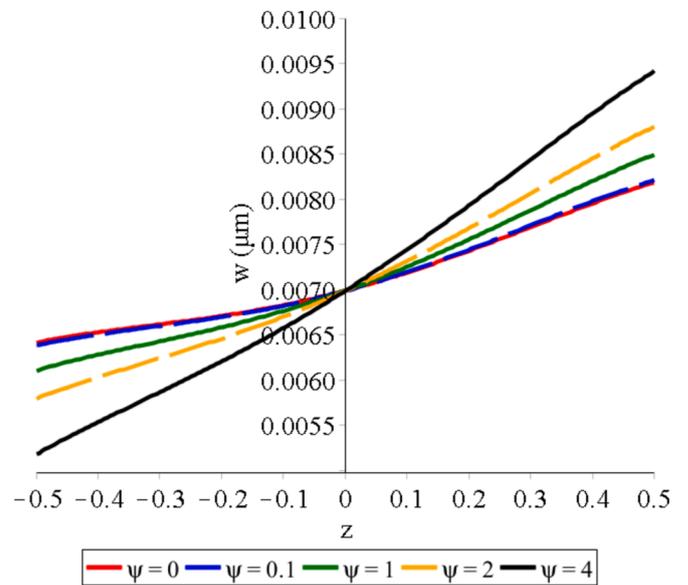

Fig. 10b. Thickness deformations vs. the different magnetic potential for CFCF.

The expressions of the presented boundary conditions in SAPM are provided here for the first time for a 3D rectangular CBS [43,44,63,66–70]

$$u(x,y,z) = \sum_{i=1}^{N} \sum_{j=1}^{M} \sum_{k=1}^{P} R_{(k+P.(j-1)+M.P.(i-1))} x^{(i-1)} y^{(j-1)} z^{(k-1)} \qquad (30a)$$

$$v(x,y,z) = \sum_{i=1}^{N} \sum_{j=1}^{M} \sum_{k=1}^{P} R_{(k+P(j-1)+M.P.(i-1)+N.M.P)} x^{(i-1)} y^{(j-1)} z^{(k-1)} \qquad (30b)$$

$$w(x,y,z) = \sum_{i=1}^{N} \sum_{j=1}^{M} \sum_{k=1}^{P} R_{(k+P(j-1)+M.P.(i-1)+2.N.M.P)} x^{(i-1)} y^{(j-1)} z^{(k-1)} \qquad (30c)$$

N, M, and P represent point distributions along the thickness and main area of the CBS.

The SAPM method can then be applied. The first step involves segmenting the region using grid points. For all three dimensions, the mesh points, as will be described in Eq. (31), conform to the extensively utilized Chebyshev-Gauss-Lobatto (CGL) grid points as

$$x_i = \frac{1}{2} L_x \left(1 - \cos \frac{i-1}{N-1} \pi \right), i = 1, 2, ..., N \qquad (31a)$$

$$y_j = \frac{1}{2} L_y \left(1 - \cos \frac{j-1}{M-1} \pi \right), j = 1, 2, ..., M \qquad (31b)$$

$$z_k = \frac{1}{2} h \left(\cos \frac{k-1}{P-1} \pi \right), k = 1, 2, ..., P \qquad (31b)$$

Fig. 3 visually depicts the CGL grid, which embraces the entire domain. Each point possesses the capability to maneuver, enabling the potential for thickness stretching, thereby manifesting the 3D displacements. Notably, the solid blue points correspond to the imposed boundaries, while the solid red points adhere to the governing equations. Non-uniformly spaced points configured by CGL enhance the accuracy owing to the proximity of boundary points. It should be pointed out that when the boundary conditions are applied, all the points in the four side surfaces must get involved with the conditions.

Given that there exist three unknown variables (u, v, and w) associated with every individual point

$$u = \begin{bmatrix} u(x_1,y_1,z_1), ..., u(x_N,y_1,z_1), u(x_1,y_1,z_2), ..., u(x_N,y_1,z_2), ..., u(x_1,y_1,z_P), ..., u(x_N,y_1,z_P) \\ u(x_1,y_2,z_1), ..., u(x_N,y_2,z_1), u(x_1,y_2,z_2), ..., u(x_N,y_2,z_2), ..., u(x_1,y_2,z_P), ..., u(x_N,y_2,z_P) \\ u(x_1,y_M,z_1), ..., u(x_N,y_M,z_1), u(x_1,y_M,z_2), ..., u(x_N,y_M,z_2), ..., u(x_1,y_M,z_P), ..., u(x_N,y_M,z_P) \end{bmatrix} \qquad (32a)$$

$$v = \begin{bmatrix} v(x_1,y_1,z_1), ..., v(x_N,y_1,z_1), v(x_1,y_1,z_2), ..., v(x_N,y_1,z_2), ..., v(x_1,y_1,z_P), ..., v(x_N,y_1,z_P) \\ v(x_1,y_2,z_1), ..., v(x_N,y_2,z_1), v(x_1,y_2,z_2), ..., v(x_N,y_2,z_2), ..., v(x_1,y_2,z_P), ..., v(x_N,y_2,z_P) \\ v(x_1,y_M,z_1), ..., v(x_N,y_M,z_1), v(x_1,y_M,z_2), ..., v(x_N,y_M,z_2), ..., v(x_1,y_M,z_P), ..., v(x_N,y_M,z_P) \end{bmatrix} \qquad (32b)$$

$$w = \begin{bmatrix} w(x_1,y_1,z_1), ..., w(x_N,y_1,z_1), w(x_1,y_1,z_2), ..., w(x_N,y_1,z_2), ..., w(x_1,y_1,z_P), ..., w(x_N,y_1,z_P) \\ w(x_1,y_2,z_1), ..., w(x_N,y_2,z_1), w(x_1,y_2,z_2), ..., w(x_N,y_2,z_2), ..., w(x_1,y_2,z_P), ..., w(x_N,y_2,z_P) \\ w(x_1,y_M,z_1), ..., w(x_N,y_M,z_1), w(x_1,y_M,z_2), ..., w(x_N,y_M,z_2), ..., w(x_1,y_M,z_P), ..., w(x_N,y_M,z_P) \end{bmatrix} \qquad (32c)$$

Fig. 10c. Thickness deformations vs. the different magnetic potential for CFFF.

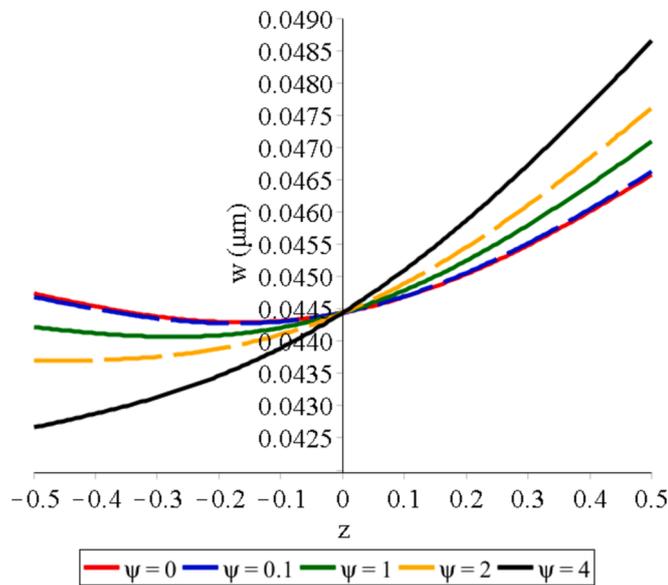**Fig. 11a.** Thickness deformations vs. length scale parameter for CFCF.

Consequently, a total of $N \times M \times P \times 3$ equations will be generated, equating to an identical number of unknowns. At last, applying the Newton-Raphson technique helps with the computation of the mentioned unknown parameters attributed to the points.

4. Results comparison

No reference has already reported the bending of smart CBS consisting of a higher-order electro-magnetic property in a 3D domain. Accordingly, by way of Fig. 4 to Fig. 7, a kind of comparison with the Abaqus commercial code has been performed to validate the present model (by removing smart properties) and the solution procedure. Then, one reaches the deflections and deformations of a thick isotropic and homogeneous rectangular CBS by the ensuing data, Fig. 5, Fig. 6.

$L_x = 20$ cm, $L_y = 10$ cm, $h = 5$ cm, $E = 190$GPa, $\nu = 0.29$.

The present semi-analytical model will be converged at $11 \times 11 \times 7$ grid points. As the current formulation is grounded on the 3D analysis, the considered validation corresponds to maximum deflections of the topmost and bottom-most surfaces of the thickness. Interestingly, it is obviously shown that the present formulation results have been in great correlation with those of 3D finite element code. Moreover, as seen by the figures, 3D elasticity gives thickness deformations very accurate.

Fig. 4 to Fig. 7 may not be sufficient to affirm the present model's precision and the solving procedure. Hence, Fig. 8 and Fig. 9 are prepared which pertain to the deflection path among the y-axis for the topmost and bottom-most layers of the CFCF CBSs. As can be marked, the deflections in both surfaces can be in an acceptable consent which confirms the further use of the present mathematical model to extract the required results.

5. Results presentation

This section is divided into some sub-sections to classify and arrange the parametric study to ease the presentation of results. Besides, in order to simplify the results, some parameters are introduced as; aspect ratio: $\beta = L_x/L_y$, thickening ratio: $H = h/L_x$. The results have been given by the following material properties,

$E = 286$GPa, $\nu = 0.32$, $a_{33} = 1.57 \times 10^{-4}$N/A^2, $h_{15} = h_{11} = h_{46} = 10^{-9}$N/A, $q_{31} = 580.3$ N/A.m, $q_{32} = q_{31}$, $q_{33} = 700$ N/A.m, $q_{15} = 275$ N/A.m.
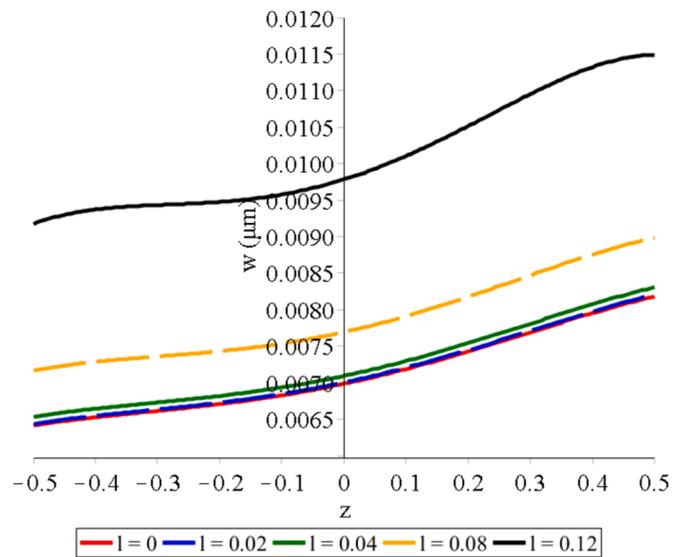
5.1. Results of magnetic potential effect

The deflections of the CBS have been investigated along the thickness due to changes in the magnetic potential with the help of Fig. 10a, Fig. 10b, and Fig. 10c are devoted to CCCC, CFCF, and CFFF boundary conditions, respectively. The input data for the three shown figures are $\beta = 0.5$, $H = 1$, $q = 1$GPa, and $l = 0.02$ μm.

If a two-dimensional CBS is examined based on the plane stress or plane strain approaches, the maximum deflection at $z = 0$ (mid-plane) is the same value at all thickness points. But, in this work, owing to the implementation of a three-dimensional analysis, according to the figures below, it is clear that the upper layers have maximum deflection and the closer we get to the lower layers of the thickness, the deflection values decrease. Finally, the least amount of deflection will be in the lowest layer of the thickness.

When the four surfaces around the CBS have zero degrees of freedom and are completely fixed and constrained, the changes in the magnetic potential cannot have a special effect on the deformation results. But, in the case that the side surfaces have degrees of freedom or are free from any moving restrictions, the effect of the magnetic potential will be greater.

An appealing result that can be taken out is that the numerical amounts of the magnetic potential underlie the deformation in the thickness of the CBS. In two-dimensional and one-dimensional problems of beams and sheets, the magnetic field leads to a change in the deflection of the CBS only, but here the magnetic field has also caused an alter in the thickness value, which shows the ability and efficiency of three-dimensional analysis to accurately solve the mechanical behavior of materials.

5.2. Results of strain gradient effect

The strain gradient effect is momentous for smart materials with high-order sensing properties. We dealt with that problem by showing Fig. 11a and Fig. 11b. Both figures are presented for changes in strain gradient parameter values and similar boundary conditions. The entrance quantities are $\beta = 0.5$, $H = 1$, and $q = 1$GPa for both figures; however, the magnetic potentials are $\psi = 0$A, and $\psi = 2$A, respectively. The first figure is designed for the case where there is no magnetic field, and in the second figure, we considered the case where a magnetic field exists with a certain amount of magnetic potential. The variations in the
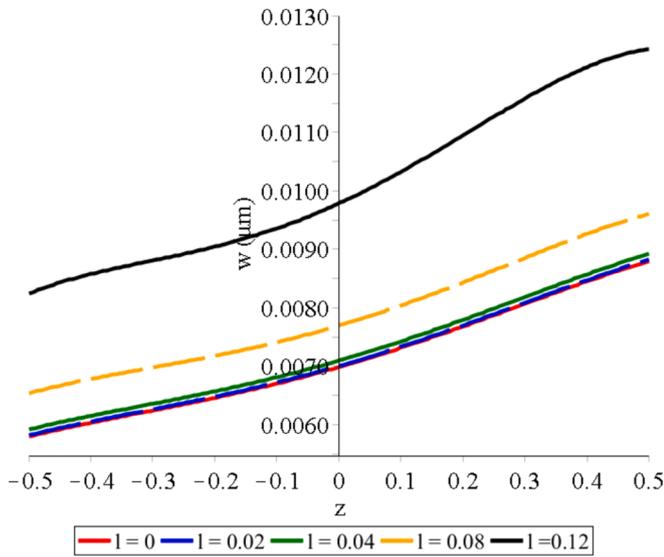
Fig. 11b. Thickness deformations vs. length scale parameter for CFCF.

Table 1

The effect of strain gradient for various boundary conditions ($L_x = 1$ μm, $L_y = 2$ μm, $h = 1$ μm, $q = 1$GPa, $\psi = 2$A).

l (μm)	Maximum deflections (μm)		
	CCCC $\times 10^{-2}$	CFCF $\times 10^{-2}$	CFFF
0.0000	0.2287	0.8552	0.1103
0.0100	0.2284	0.8555	0.1113
0.0200	0.2276	0.8567	0.1146
0.0300	0.2264	0.8594	0.1208
0.0400	0.2247	0.8648	0.1316
0.0500	0.2228	0.8742	0.1509
0.0525	0.2223	0.8774	0.1578
0.0550	0.2218	0.8808	0.1660
0.0575	0.2213	0.8847	0.1756
0.0600	0.2208	0.8888	0.1869
0.0625	0.2203	0.8933	0.1998
0.0650	0.2198	0.8981	0.2144
0.0675	0.2192	0.9031	0.2307
0.0700	0.2185	0.9082	0.2485
0.0725	0.2175	0.9133	0.2708
0.0750	0.2160	0.9180	0.3292
0.0760	0.2151	0.9196	0.4809

Fig. 12a. Effect of thickness deformation along the x-axis for CFCF.

deflection along the dimensionless thickness show that the strain gradient parameter is a very influential factor in the mechanical behavior of the smart CBSs. In very small values of the strain gradient parameter, the difference in the deflection is not so noticeable. However, when the value of this parameter goes up, how the thickness deforms will change. This result can make perfect sense, from a physical point of view. Since the strain gradient is the result of changes in strains, and strains are dimensionally dependent, in a three-dimensional analysis, the effect of variations in the third dimension (thickness) is also included in the problem. Therefore, the strain gradient will become more dominant due to the embracing of ε_z in the equations. On the other side, by collating both figures it can be observed that the slope of the curves is more steep in Fig. 11b which shows that the ratio of deflections in the upper layers to the lower layers of the thickness is in a further difference. This valuable finding stems from the magnetic potential influence and its impact on the thickness deformation.

In order to provide comparable results, some numeric results are tabulated via Table 1. The Table is figured out for three different boundary conditions, namely CCCC, CFCF, and CFFF. The input data are given numeral, including the dimensional quantities.

5.3. Results of the effect of thickness deformation in rectangular CBSs

Fig. 12a, Fig. 12b, Fig. 12c, Fig. 12d, Fig. 12e, and Fig. 12f, are state-of-the-art in the field of mechanics of smart materials. The details of the inputs are $\beta = 0.5$, $H = 1$, and $q = 1$GPa for all six indicated figures. Though the values of the strain gradient parameter are respectively, $l = 0.02$ μm, $l = 0.02$ μm, $l = 0.02$ μm, and $l = 0.02$ μm for the first four figures, and the values of the magnetic potential are respectively, $\psi = 0$A and $\psi = 2$A.

Let us initially nominate a parameter by which one could define the deflection in the topmost layer of the thickness to that of the bottom-most. In point of fact, it presents the thickness deformation ratio as

$$W_S = \frac{w_{Topmostsurface}}{w_{Bottom-mostsurface}}$$

The first two diagrams are allocated for CFCF boundary conditions and the rest belong to the CFFF. The main objective of the diagrams is to assess the W_S parameter in conjunction with the x and y axes while the value of the magnetic potential differs. It is worth mentioning that for CFCF, $y = 0,2$ are fully clamped and for CFFF, $y = 0$ is fully free and $y = 2$

stands for totally clamped. But, $x = 0,1$ are completely free for both CFCF and CFFF. Let us here point out that the real start and end points of these four diagrams and the others showing thickness deformation in line with the dimensionless length and width of the CBS are not what is shown in the figures. As a matter of fact, there is an asymptote for these items at $x = 0,1$ and $y = 0,2$ for the clamped boundary condition that W_S would lean towards 0. Thus, we would like to allow ourselves to hold forth on 0.000001 instead of 0, and 0.999999 in place of 1. An impressive result of these figures is that the W_S parameter is a big deal near the center of the y dimension when $y = 0,2$. The deflections close to free edges ($x = 0,1$ for all cases, and $y = 0$ for the CFFF) give smaller values for W_S compared to fully fixed conditions. Additionally, the magnetic potential causes the W_S parameter more noteworthy. This substantial outcome has been attained in the previous figures as well.

5.4. Results of the effect of thickness deformation in square CBSs

This part of the results of the article is dedicated to smart square CBSs. This section is a continuation of the previous section with all the same conditions and inputs, but the previous section was related to rectangular CBSs. In the discussion of rectangular sheets, we observed
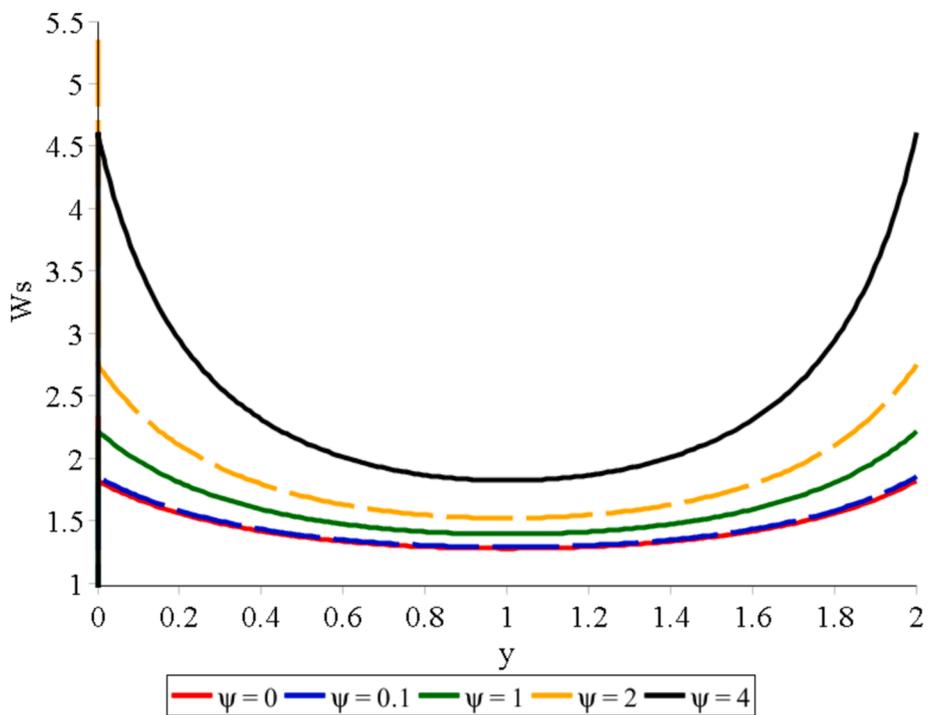
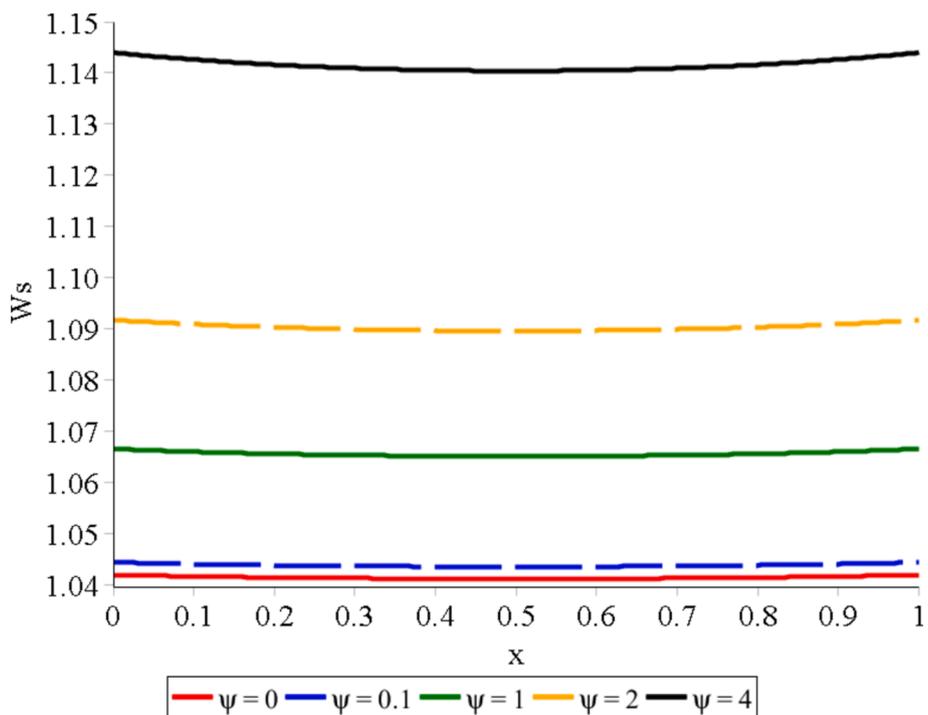**Fig. 12b.** Effect of thickness deformation along the y-axis for CFCF.

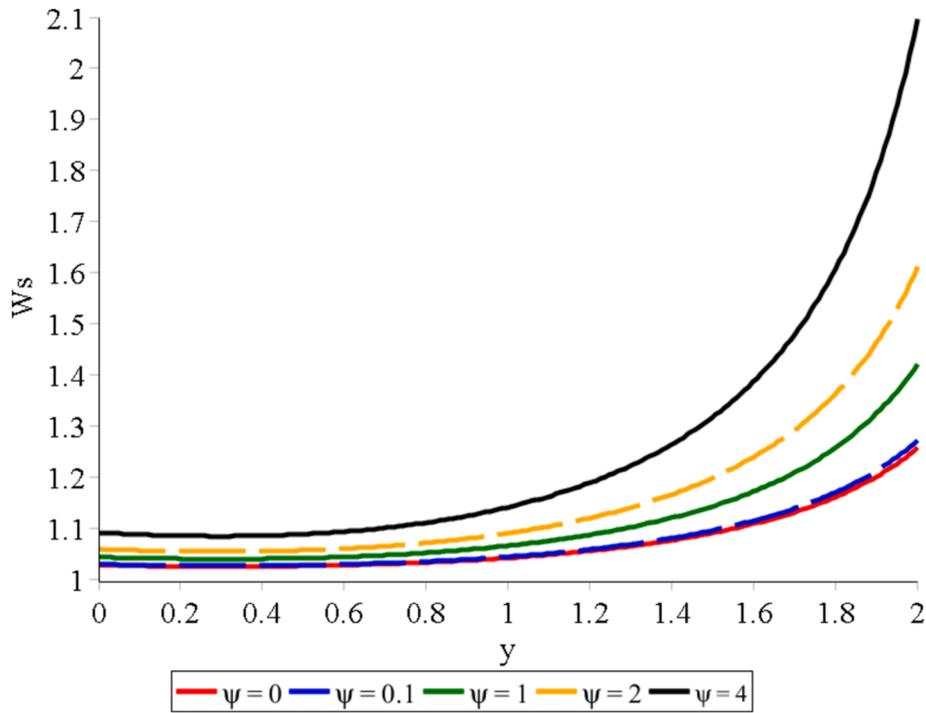**Fig. 12c.** Effect of thickness deformation along the x-axis for CFFF.

Fig. 12d. Effect of thickness deformation along the y-axis for CFFF.
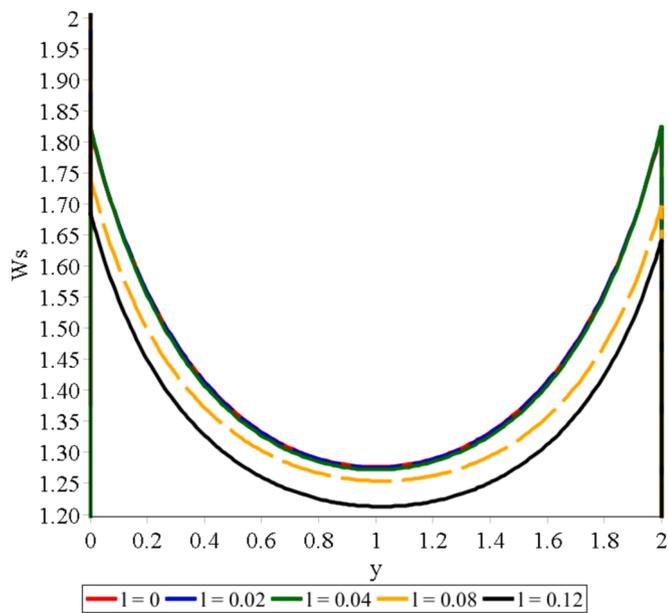

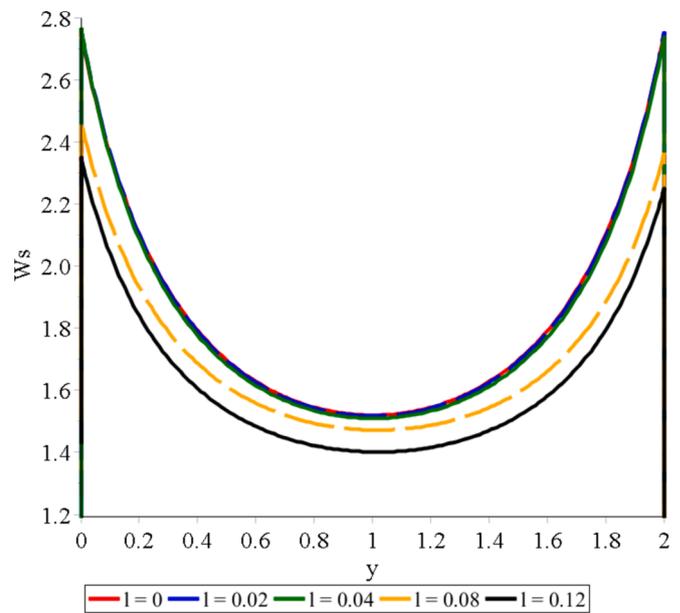**Fig. 12e.** Effect of thickness deformation along the y-axis for CFCF.

Fig. 12f. Effect of thickness deformation along the x-axis for CFCF.

that the changes of the W_S parameter in both the x and y axes are different for both CCCC and CFCF boundary conditions, and here we are going to check this issue for square CBSs by drawing Fig. 13a, Fig. 13b, Fig. 13c, and Fig. 13d. Let us use the following quantities $\beta = 0.5$, $H = 1$, $q = 1\text{GPa}$, and $l = 0.02\ \mu\text{m}$ for the discussed figures.

Since the studied smart CBS is completely isotropic, therefore, we should see the same changes for the W_S in the square CBS. This means that the thickness of the CBS is deformed equally on both edges. Finally, by presenting these figures, it is clear that this hypothesis cannot be

absolutely correct. If all four sides of the CBS have the same boundary conditions, the W_S parameter will be similar in the direction of x and y dimensions, which Fig. 13a and Fig. 13b display this result. But in Fig. 13c and Fig. 13d, one can see that the variations of the W_S are different in the x and y axes.

5.5. Results of 3D plates vs. 3D beams

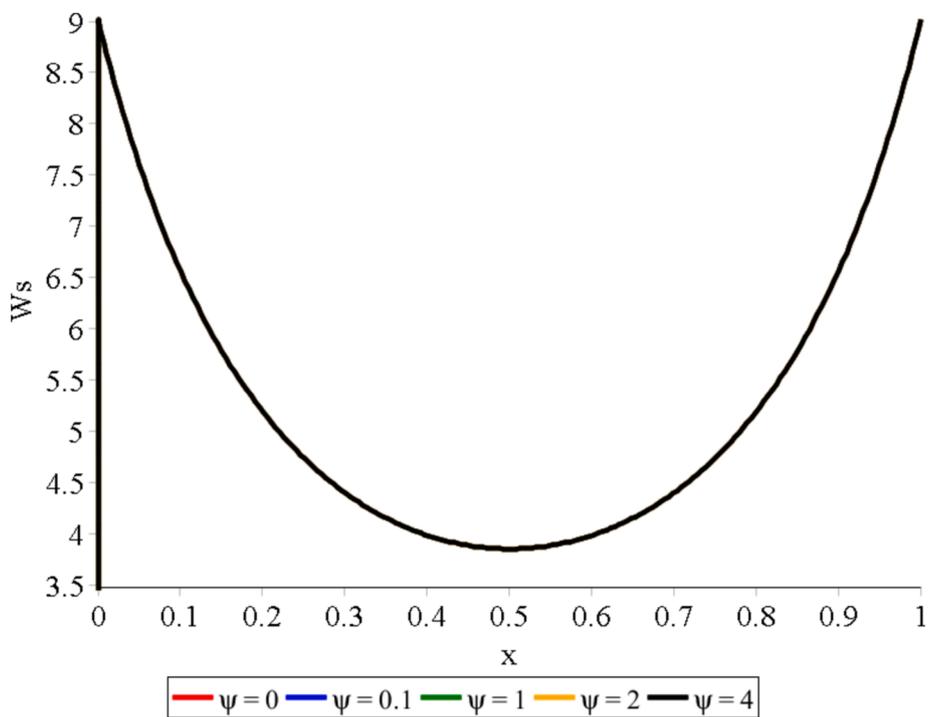The last part of the discussion section investigates a comparison

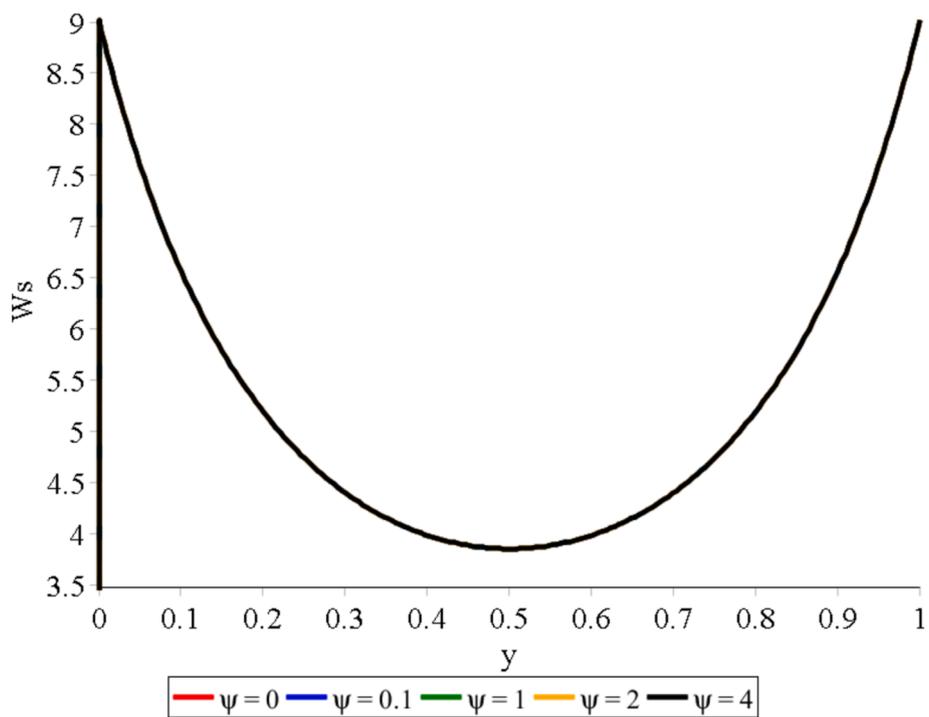**Fig. 13a.** Effect of thickness deformation along the x-axis for CCCC.

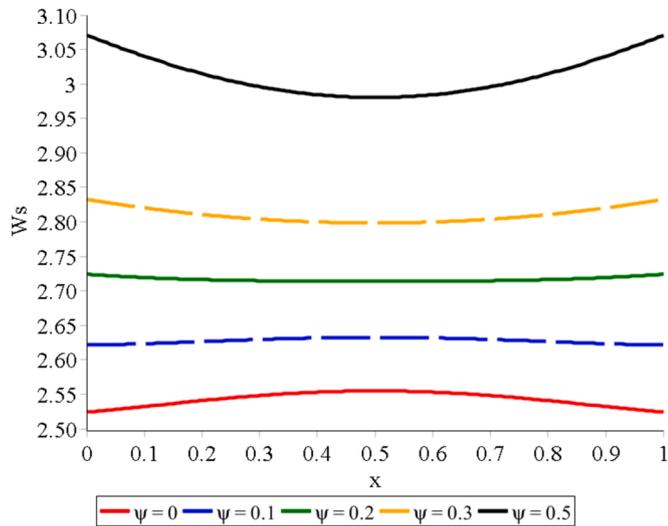**Fig. 13b.** Effect of thickness deformation along the y-axis for CCCC.

Fig. 13c. Effect of thickness deformation along the x-axis for CFCF.

Fig. 14. Comparison of the deflection through the thickness of the thick CBS with CFCF.

between the 3D plates (fully 3D) and a 3D beam ($d/dy = 0$) through Fig. 14 utilizing $\beta = 0.5$, $H = 1$, $q = 1\mathrm{GPa}$, $\psi = 2A$, $l = 0.02\ \mu m$. As it is vivid, the results of the 3D plate at the mid-length ($x1 + 0.5 \times x2$) coincide with the results of the 3D beam; however, the results of the 3D plate at the $x = 0$ (edge) deviate. This fact simply indicates that the edge effect is a notable factor in 3D elasticity studies and a full 3D analysis supplies more precise mechanical behavior.

6. Conclusions

Several key results emerged from this comprehensive investigation into the effects of lower- and higher-order smart properties within a fully three-dimensional mechanical analysis. Prior to this study, no examination of the three-dimensional (3D) elasticity of the smart PFM composite CBS had been undertaken, as affirmed by an exhaustive review of existing literature. Consequently, it was evident that further scrutiny
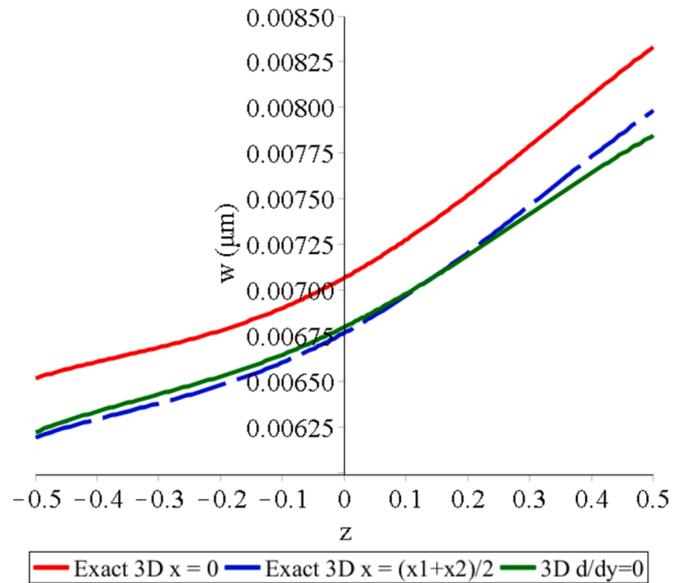
was imperative. To facilitate this analysis, the governing equations were tailored to incorporate the term $\partial/\partial z$ denoting the thickness stretching effect. Revisiting a higher-level magnetic model previously proposed and confined to piezomagnetic structures, this study adapted and amalgamated various methodologies such as a 3D CBS kinematic model, Hamilton's principle, von Kármán strain nonlinearity, and specific reverse magnetic models to derive the governing equations for a thick composite CBS. The resulting necessary tensors have been expressed in 3D configurations pertinent to a comprehensive three-dimensional analysis. Subsequently, the derived linear three-dimensional equations characterized the bending behavior of the smart plate which have been moved into a 3D semi-analytical Polynomial Method to advance essential parametric studies. Beyond merely uncovering specific findings
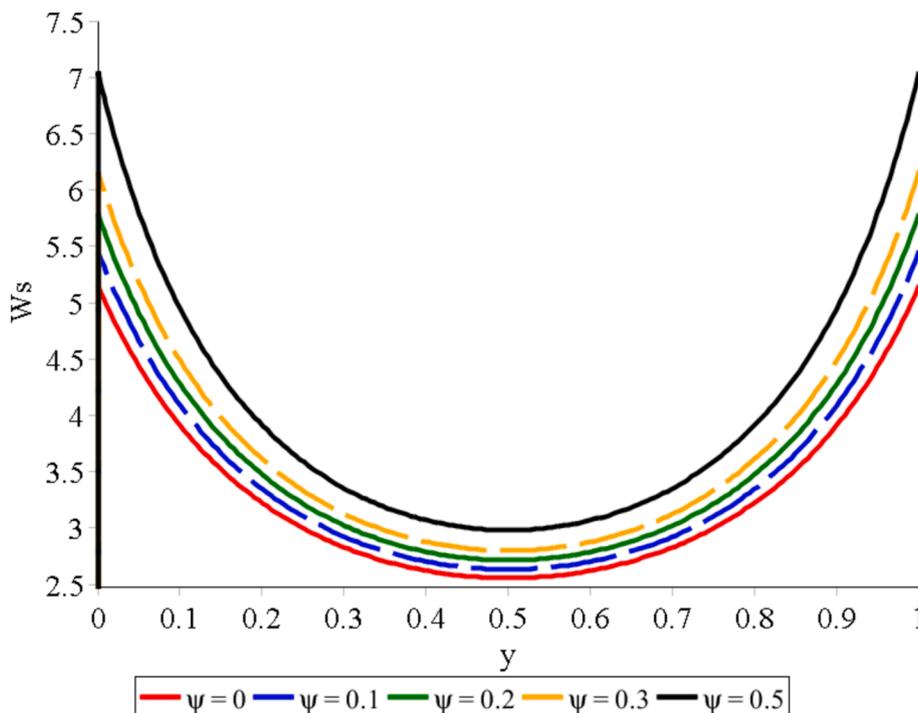

Fig. 13d. Effect of thickness deformation along the y-axis for CFCF.

outlined below, this work underscored the significance of conducting 3D mechanical analyses that integrate various physical connections, particularly the interplay involving FM, thereby illuminating fresh insights into PFM dynamics.

- *In the mechanical analysis of three-dimensional CBSs, one of the influential and determining parameters can be the deflection ratio defining deflections in the highest thickness layer to the lowest one for CBS (W_S). The value of this parameter in two-dimensional elasticity analysis is equal to one. Because in such problems there is no thickness deformation after applying static or dynamic loads, and the thickness remains constant. But in the three-dimensional elasticity, the main discussion of this article, the value of this parameter was meaningful in some conditions. For example, the value of the W_S parameter becomes a relatively large number when the smart CBS is in the clamped boundary condition.*

- *In two-dimensional elasticity, many parameters affect the behavior of smart CBSs. However, it is unfeasible to check the effect of such parameters on the thickness change. Nevertheless, in the three-dimensional elasticity and as a result of the computational modeling obtained in this study, it was found that parameters such as magnetic potential and strain gradient have a direct effect on the thickness deformation.*

- *A fully three-dimensional elasticity analysis shows that the edge effect can be a strong player in predicting the mechanical response of smart structures.*

CRediT authorship contribution statement

Mohammad Malikan: Writing – review & editing, Writing – original draft, Validation, Methodology, Investigation, Data curation, Conceptualization. **Shahriar Dastjerdi:** Writing – review & editing, Visualization, Validation, Software, Methodology, Investigation, Formal analysis, Data curation. **Victor A. Eremeyev:** Writing – review & editing, Supervision, Methodology, Investigation, Formal analysis, Conceptualization. **Mehran Kadkhodayan:** Writing – review & editing, Methodology, Investigation, Formal analysis.

Declaration of competing interest

The authors declare that they have no known competing financial interests or personal relationships that could have appeared to influence the work reported in this paper.

Acknowledgements

Data availability

Data will be made available on request.

References

[1] Chen Q, Du X, Wang W, Chatzigeorgiou G, Meraghni F, Zhao G. Isogeometric homogenization of viscoelastic polymer composites via correspondence principle. Compos Struct 2023;323:117475.

[2] Dastjerdi Sh, Akgöz B. New static and dynamic analyses of macro and nano FGM plates using exact three-dimensional elasticity in thermal environment. Compos Struct 2018;192:626–41.

[3] Karami B, Ghayesh MH. Vibration characteristics of sandwich microshells with porous functionally graded face sheets. Int J Eng Sci 2023;189:103884.

[4] Mohamed ASY. Smart Materials Innovative Technologies in architecture. Towards Innovative design paradigm Energy Procedia 2017;115:139–54.

[5] Gia Phi B, Van Hieu D, Sedighi HM, Sofiyev AH. Size-dependent nonlinear vibration of functionally graded composite micro-beams reinforced by carbon nanotubes with piezoelectric layers in thermal environments. Acta Mechanica 2022;233:2249–70.

[6] Yang W, Liu M, Chen S, Kang W, Chen J, Li Y. Electromechanical analysis of a self-sensing torsional micro-actuator based on CNTs reinforced piezoelectric composite with damage. Compos Struct 2023;313:116945.

[7] Ezzin H, Mkaoir M, Qian Z, Arefi M, Das R. Lamb Wave Analysis in Anisotropic Multilayer Piezoelectric-piezomagnetic Material. J Appl Comput Mech 2022;8:629–40.

[8] Qilin J. Electro-mechanical analysis of functionally graded graphene reinforced composite laminated plate with macro fiber composite actuator. Compos Struct 2023;319:117132.

[9] Vijay K, Varadan K, Vinoy J, Gopalakrishnan S. Smart material systems and mems: design and development methodologies. John Wiley & Sons; 2006.

[10] Jankowski P. Detection of nonlocal calibration parameters and range interaction for dynamics of FGM porous nanobeams under electro-mechanical loads. F U Mech Eng 2022;20:457–78.

[11] Ud Din I, Aslam N, Medhin Y, Sikandar Bathusha MS, Irfan MS, Umer R, et al. Electromechanical behavior of self-sensing composite sandwich structures for next generation more electric aerostructures. Compos Struct 2022;300:116169.

[12] Silva MR, Tita V, Medeiros RD. Influence of the geometric parameters on the effective properties of piezoelectric composite sensors using real measurements and a new RVE. Compos Struct 2023;303:116292.

[13] Singhal A, Sedighi HM, Ebrahimi F, Kuznetsova I. Comparative study of the flexoelectricity effect with a highly/weakly interface in distinct piezoelectric materials (PZT-2, PZT-4, PZT-5H, LiNbO3, BaTiO3). Waves Random Complex 2021;31:1780–98.

[14] Fattahi I, Mirdamadi HR. Novel composite finite element model for piezoelectric energy harvesters based on 3D beam kinematics. Compos Struct 2017;179:161–71.

[15] Mallek-Zouari I, Ben Taazayet W, Grenèche JM, Bessais L, Dkhil B, Thabet MN. Field-induced spin cycloidal modulation to antiferromagnetic transition and possible flexomagnetic effect in BiFeO3 nanoparticles. J Alloy Comp 2023;934:167944.

[16] Borkar H, Gaikwad VM, Choudhary RJ, Tomar M, Gupta V, Kumar A. Flexomagnetic effects on inhomogeneously strained multiferroics composites. J Mag Mag Mater 2022;553:169274.

[17] Makushko P, Kosub T, Pylypovskyi OV, et al. Flexomagnetism and vertically graded Néel temperature of antiferromagnetic Cr2O3 thin films. Nat Commun 2022;13:6745.

[18] Hong Lee J, Kim KE, Jang BK, Ünal AA, Valencia S, Kronast F, et al. Strain-gradient-induced magnetic anisotropy in straight-stripe mixed-phase bismuth ferrites: Insight into flexomagnetism. Phys Rev B 2017;96:064402.

[19] Eliseev EA, Morozovska AN, Glinchuk MD, Blinc R. Spontaneous flexoelectric/flexomagnetic effect in nanoferroics. Phys Rev B 2009;79:165433.

[20] Eliseev EA, Glinchuk MD, Khist V, Skorokhod VV, Blinc R, Morozovska AN. Linear magnetoelectric coupling and ferroelectricity induced by the flexomagnetic effect in ferroics. Phys Rev B 2011;84:174112.

[21] Eliseev EA, Morozovska AN, Khist VV, Polinger V. Chapter Six - Effective flexoelectric and flexomagnetic response of ferroics, Editor(s): Robert L. Stamps, Helmut Schultheiß, Solid State Physics, Academic Pre 2019;70:237–89.

[22] Kabychenkov AF, Lisovskii FV. Flexomagnetic and flexoantiferromagnetic effects in centrosymmetric antiferromagnetic materials. Tech Phys 2019;64:980–3.

[23] Sabirianov RF, Lukashev P. Magneto-elastic properties of frustrated triangular magnetic structure: flexomagnetic effect. American Physical Society, APS March Meeting 2010. abstract id. Q34.008.

[24] Lukashev P, Sabirianov RF. Flexomagnetic effect in frustrated triangular magnetic structures. Phys Rev B 2010;82:094417.

[25] Malikan M. On mechanics of piezocomposite shell structures. Int J Eng Sci 2024;198:104056.

[26] Khabisi-Momeni H, Tahani M. A size-dependent study on buckling and post-buckling behavior of imperfect piezo-flexomagnetic nano-plate strips. Adv nano res 2022;12:427–40.

[27] Malikan M, Eremeyev VA. The effect of shear deformations' rotary inertia on the vibrating response of multi-physic composite beam-like actuators. Compos Struct 2022;297:115951.

[28] Malikan M, Eremeyev VA. On a flexomagnetic behavior of composite structures. Int J Eng Sci 2022;175:103671.

[29] Malikan M, Eremeyev VA. Flexomagnetic response of buckled piezomagnetic composite nanoplates. Compos Struct 2021;267:113932.

[30] Malikan M, Eremeyev VA. Effect of surface on the flexomagnetic response of ferroic composite nanostructures; nonlinear bending analysis. Compos Struct 2021;271:114179.

[31] Sladek J, Sladek V, Xu M, Deng Q. A cantilever beam analysis with flexomagnetic effect. Meccanica 2021;56:2281–92.

[32] Zhang N, Zheng Sh, Chen D. Size-dependent static bending of flexomagnetic nanobeams. J Appl Phys 2019;126:223901.

[33] Zhang N, Zheng S, Chen D. Size-dependent static bending, free vibration and buckling analysis of curved flexomagnetic nanobeams. Meccanica 2022;57: 1505–18.

[34] Sidhardh S, Ray MC. Flexomagnetic response of nanostructures. J Appl Phys 2018; 124:244101.

[35] Malikan M, Dastjerdi Sh, Eremeyev VA, Sedighi HM. On a 3D material modelling of smart nanocomposite structures. Int J Eng Sci 2023;2023(193):103966.

[36] Zheng Y, Karami B, Shahsavari D. On the vibration dynamics of heterogeneous panels under arbitrary boundary conditions. Int J Eng Sci 2022;178:103727.

[37] Karami B, Janghorban M, Fahham H. On the stress analysis of anisotropic curved panels. Int J Eng Sci 2022;172:103625.

[38] Xu X, Karami B, Janghorban M. On the dynamics of nanoshells. Int J Eng Sci 2021; 158:103431.

[39] Malikan M, Krasheninnikov M, Eremeyev VA. Torsional stability capacity of a nano-composite shell based on a nonlocal strain gradient shell model under a three-dimensional magnetic field. Int J Eng Sci 2020;148:103210.

[40] Alshenawy R, Sahmani S, Safaei B, Elmoghazy Y, Al-Alwan A, Al NM. Three-dimensional nonlinear stability analysis of axial-thermal-electrical loaded FG piezoelectric microshells via MKM strain gradient formulations. Appl Math Comput 2023;439:127623.

[41] Dastjerdi Sh, Malikan M, Dimitri R, Tornabene F. Nonlocal elasticity analysis of moderately thick porous functionally graded plates in a hygro-thermal environment. Compos Struct 2021;255:112925.

[42] Malikan M, Nguyen VB. Buckling analysis of piezo-magnetoelectric nanoplates in hygrothermal environment based on a novel one variable plate theory combining with higher-order nonlocal strain gradient theory. Phys E: Low-dimens Syst Nanostructures 2018;102:8–28.

[43] Dastjerdi Sh, Akgöz B, Civalek Ö. On the effect of viscoelasticity on behavior of gyroscopes. Int J Eng Sci 2020;149:103236.

[44] Dastjerdi Sh, Akgöz B, Civalek Ö, Malikan M, Eremeyev VA. On the non-linear dynamics of torus-shaped and cylindrical shell structures. Int J Eng Sci 2020;56: 103371.

[45] Dastjerdi Sh, Akgöz B, Civalek Ö. On the shell model for human eye in Glaucoma disease. Int J Eng Sci 2021;158:103414.

[46] Ueltschi TW. (2014). Third-Order Tensor Decompositions and Their Application in Quantum Chemistry.РеЖиМ доступа: http://buzzard. ups. edu/courses/ 2014spring/420projects/math420-UPS-spring-2014-ueltschi-tensors-in-chemistry. pdf.

[47] Zhang YW, She GL, Ding HX. Nonlinear resonance of graphene platelets reinforced metal foams plates under axial motion with geometric imperfections. Eur J Mech A-Solid 2023;98:104887.

[48] Shahmohammadi MA, Mirfatah SM, Salehipour H, Civalek Ö. On nonlinear forced vibration of micro scaled panels. Int J Eng Sci 2023;182:103774.

[49] Naskar S, Shingare KB, Mondal S, Mukhopadhyay T. Flexoelectricity and surface effects on coupled electromechanical responses of graphene reinforced functionally graded nanocomposites: A unified size-dependent semi-analytical framework. Mech Syst Signal Pr 2022;169:108757.

[50] Zhang GY, Guo ZW, Gao QYL, XL, Jin F.. A new model for thermal buckling of an anisotropic elastic composite beam incorporating piezoelectric, flexoelectric and semiconducting effects. Acta Mechanica 2022;233:1719–38.

[51] Qu Y, Jin F, Yang J. Torsion of a flexoelectric semiconductor rod with a rectangular cross section. Arch Appl Mech 2021;91:2027–38.

[52] Shu L, Wei X, Pang T, Yao X, Wang C. Symmetry of flexoelectric coefficients in crystalline medium. J Appl Phys 2011;110:104106.

[53] Stempin P, Sumelka W. Space-fractional small-strain plasticity model for microbeams including grain size effect. Int J Eng Sci 2022;175:103672.

[54] Stempin P, Pawlak TP, Sumelka W. Formulation of non-local space-fractional plate model and validation for composite micro-plates. Int J Eng Sci 2023;192:103932.

[55] Dastjerdi Sh, Jabbarzadeh M. Non-linear bending analysis of multi-layer orthotropic annular/circular graphene sheets embedded in elastic matrix in thermal environment based on non-local elasticity theory. Appl Math Model 2017; 41:83–101.

[56] Yurkov AS, Yudin PV. Continuum model for converse flexoelectricity in a thin plate. Int J Eng Sci 2023;182:103771.

[57] Torabi J, Niiranen J, Ansari R. Nonlinear finite element analysis within strain gradient elasticity: Reissner-Mindlin plate theory versus three-dimensional theory. Eur J Mech A-Solid 2021;87:104221.

[58] Gusev AA, Lurie SA. Symmetry conditions in strain gradient elasticity. Math Mech Solids 2017;22:683–91.

[59] Zhou Sh, Li A, Wang B. A reformulation of constitutive relations in the strain gradient elasticity theory for isotropic materials. Int J Solids Struct 2016;80:28–37.

[60] Auffray N, Le Quang H, He QC. Matrix representations for 3D strain-gradient elasticity. J Mech Phys Solids 2013;61:1202–23.

[61] Sahmani S, Safaei B. Nonlinear three-dimensional oscillations of probabilistic reinforced nanocomposite shells at microscale via modified strain gradient meshfree formulations. P I Mech Eng C-J Mec 2022;237.

[62] Abouelregal AE, Sedighi HM, Faghidian SA, Shirazi AH. Temperature-dependent physical characterisitcs of the rotating nonlocal nanobeams subject to a varying heat source and a dynamic load. Facta Univ, Ser Mech Eng 2021;19:633–56.

[63] Dastjerdi Sh, Malikan M, Akgöz B, Civalek Ö, Wiczenbach T, Eremeyev VA. On the deformation and frequency analyses of SARS-CoV-2 at nanoscale. Int J Eng Sci 2022;170:103604.

[64] Malikan M, Tornabene F, Dimitri R. Nonlocal three-dimensional theory of elasticity for buckling behavior of functionally graded porous nanoplates using volume integrals. Mater Res Express 2018;5:095006.

[65] Zafarmand H, Kadkhodayan M. Three dimensional elasticity solution for static and dynamic analysis of multi-directional functionally graded thick sector plates with general boundary conditions. Compos Part B-Eng 2015;69:592–602.

[66] Dastjerdi Sh, Akgöz B. On the statics of fullerene structures. Int J Eng Sci 2019;142: 125–44.

[67] Dastjerdi Sh, Naeijian F, Akgöz B, Civalek Ö. On the mechanical analysis of microcrystalline cellulose sheets. Int J Eng Sci 2021;166:103500.

[68] Dastjerdi Sh, Malikan M, Tadi BY. A comprehensive study on nonlinear hygro-thermo-mechanical analysis of thick functionally graded porous rotating disk based on two quasi-three-dimensional theories. Mech Based Des Struct 2022;50: 3596–625.

[69] Dastjerdi Sh, Alibakhshi A, Akgöz B, Civalek Ö. On a comprehensive analysis for mechanical problems of spherical structures. Int J Eng Sci 2023;183:103796.

[70] Dastjerdi Sh, Civalek Ö, Malikan M, Akgöz B. On analysis of nanocomposite conical structures. Int J Eng Sci 2023;191:103918.